A Static Aeroelastic Analysis of a Flexible Wing Mini Unmanned Aerial Vehicle

THESIS

Nathan A. Pitcher, Captain, USAF

AFIT/GAE/ENY/08-M23

DEPARTMENT OF THE AIR FORCE
AIR UNIVERSITY

AIR FORCE INSTITUTE OF TECHNOLOGY

Wright-Patterson Air Force Base, Ohio

The views expressed in this thesis are those of the author and do not reflect the official policy or position of the United States Air Force, Department of Defense, or the United States Government.

AFIT/GAE/ENY/08-M23

A Static Aeroelastic Analysis of a Flexible Wing Mini Unmanned Aerial Vehicle

THESIS

Presented to the Faculty

Department of Aeronautical and Astronautical Engineering

Graduate School of Engineering and Management

Air Force Institute of Technology

Air University

Air Education and Training Command

In Partial Fulfillment of the Requirements for the

Degree of Master of Science in Aeronautical Engineering

Nathan A. Pitcher, BS

Captain, USAF

March 2008

AFIT/GAE/ENY/08-M23

A Static Aeroelastic Analysis of a Flexible Wing Mini Unmanned Aerial Vehicle

Nathan A. Pitcher, BS

Captain, USAF

Approved:

/signed/	14 March 2008
Lt Col R. C. Maple, PhD (Chairman)	date
/signed/	14 March 2008
Dr. M. F. Reeder (Member)	date
/signed/	14 March 2008
Dr. J. T. Black (Member)	date

Abstract

The static aeroelastic behavior of the Nighthawk mini unmanned aerial vehicle is examined using a combined experimental and computational approach. Three wings are examined. In order of increasing stiffness they are: a flexible wing, a stiff wing, and a fictitious rigid wing with zero deflection. Photogrammetry is used during wind tunnel testing to measure the average deflected shape of the flexible and stiff wings during flight. The independent variables during wind tunnel tests are angle of attack (ranging from -5.1° through 13.4°) and velocity, which is 20 mph, 30 mph, and 40 mph. Roll angle and yaw angle are control variables, held constant at 0°. The measured deflection of each wing is used to adjust the wing shape for computational fluid dynamics analysis. Solutions are obtained for the flexible, stiff, and undeflected (or rigid) wings using a steady-state viscous flow solver with a Spalart-Allmaras turbulence model. The flexible and stiff wings experience two forms of deformation during flight. They bend upward along the span increasing the dihedral, and the leading edge twists downward (wing washout). The amplitude of deflection is greatest for the flexible wing. As a result, the flexible wing is more stable, but also exhibits worse static aerodynamic performance. The rigid wing has the greatest lift ($C_{L\ max} = 1.29$) and the highest lift-to-drag ratio ($\frac{L}{D}_{max} = 10.2$). Stall occurs first near the root for all three wings. None of the wings stall at the tip in the range of angles of attack tested. A separation bubble forms under the wing at angles of attack less than 8°. This separation decreases the overall lift. It is most prominent on the flexible wing.

Acknowledgements

There are many who deserve credit for their contributions to this work. I would like to thank my advisor, Lt Col Raymond Maple, for his support and expert advice. His feedback improved the quality of the document immeasurably. Dr. Jonathan Black tutored me in photogrammetry. Dr. Mark Reeder was a fountain of knowledge in wind tunnel experimentation. Mr. Jay Anderson introduced me to the lab and equipment. Mr. Chris Zickefoose helped prepared the model for wind tunnel testing. Dr. Mark Reeder, Mr. John Hixenbaugh, and Ms. Tina Reynolds all assisted with wind tunnel operation. I would like to thank my friends in the Linux Lab Mr. Aaron McClung, Capt Abram Claycomb, Capt Darrell Crowe, Capt Jason Lee, and Lt Michael Bartowitz for their comradery, friendship, and helpful advice. I would like to thank the sponsoring organization AFRL/RBCA for the opportunity to work on this fascinating project. I would also like to thank the developers of the Nighthawk, Applied Research Associates, for supplying the test model and CAD data. Specifically, Alan Lawson and Adam Ferguson have been extremely helpful.

Finally, I would like to thank my family. My parents instilled good values and work ethic at a young age, which prepared me for this and many other life experiences. My children are a constant reminder of the most important aspect of life. My dear wife has cheerfully accepted tremendous personal sacrifice to support me in every endeavor.

Nathan A. Pitcher

Table of Contents

Page

List of Figures

List of Tables

List of Symbols

Symbol		Page
C_L	Lift Coefficient	14
α	Angle of Attack	14
$C_{L\ max}$	Maximum lift coefficient	14
C_D	Drag Coefficient	15
L	Lift	17
ρ_∞	Freestream Density	17
v_∞	Freestream Velocity	17
S	Wing Planform Area	17
D	Drag	17
$C_{L\ \alpha}$	Lift Curve Slope	18
$C_{l\ \alpha}$	Lift Curve Slope of a 2-D Airfoil	18
e	Oswald Wing Efficiency Factor	18
C_{D0}	Parasite Drag	18
C_{Dind}	Induced Drag	18
C_{DM}	Wave Drag	18
$\frac{L}{D}$	Lift-to-Drag Ratio	18
δ_{99}	99% boundary layer thickness	44
x	Length along the flat plate	44
Re_x	Reynolds Number based on x	44
$C_{L\alpha}$	Change in lift coefficient with angle of attack	48
$C_{M\alpha}$	Change in moment coefficient with angle of attack	48
u	Velocity in the x-direction (stream-wise).	56

List of Abbreviations

A Static Aeroelastic Analysis of a Flexible Wing Mini Unmanned Aerial Vehicle

I. Introduction

1.1 Background

Unmanned Aerial Vehicles (UAV) are aircraft with a host of potential military and civilian applications. The size of currently fielded UAVs is widely varied with wingspans ranging from 7 inches to 130 ft [7]. Mini-UAVs currently in the field have wingspans ranging from 21 inches to 10 ft. The predominant mission for these mini-UAVs is surveillance and reconnaissance. They carry a variety of payloads including infrared cameras, television cameras and jamming electronics. Potential military applications for mini-UAVs include local reconnaissance, target identification, post-strike battle damage assessment, electronic warfare (including radar jamming), and combat search and rescue [18]. Potential civilian applications include monitoring traffic, inspection of oil pipelines or power-lines, border surveillance, killing harmful insects, surveying wildlife, real estate photography, monitoring concentrations in chemical spills, and more [18].

The Nighthawk mini-UAV was designed for aerial surveillance. It has a removable wing (26 inch span) that can be stored in-line with the aircraft. The Nighthawk has a Global Positioning System (GPS) receiver just behind the nose and a removable hull for easy access to the payload (cameras).

Two improvements are being implemented to the original Nighthawk design. First, the flexible wing is being replaced with a stiffer wing that has less deflection during flight. Second, control algorithms are being developed to enable deployment of co-operative swarms of semi-autonomous Nighthawk mini-UAVs.

The Nighthawk is similar to another UAV called the Battlefield Air Targeting Camera (BATCAM). The BATCAM is a mini-UAV used by Air Force Special Operations Command (AFSOC) personnel to increase situational awareness in the battlefield [7]. A significant feature of the BATCAM is its portability. It has a flexible reflex wing (24 inch span) that can be rolled under the belly enabling easy transportation in a tube. Since the Nighthawk and the BATCAM are similar, the studies of the BATCAM performed by DeLuca [11] and Gamble [17] are valuable references for the current study of the Nighthawk. Figure 1.1 contains photos of the BATCAM and the Nighthawk.

(a) Original BATCAM with reflex wing [10].

(b) Nighthawk, top view.

(c) Nighthawk, side view.

Figure 1.1: Evolution of the Nighthawk mini-UAV.

1.2 Motivation

Since the Nighthawk will be operated in swarms, the control algorithm is of utmost importance to mission accomplishment. The control algorithm is based on linearized performance characteristics of the aircraft. These performance characteristics are not explicitly known and have changed with each development cycle of the aircraft. A better understanding of the performance characteristics of the Nighthawk is desired in order to improve the fidelity of the control model.

This thesis illuminates the effect of a flexible wing on the pitch performance of the aircraft. The Nighthawk mini-UAV is studied with both the second generation wing (referred to as flexible wing), the stiffer current wing (referred to as stiff wing), and a fictitious wing with no deflection (referred to as rigid wing). The lift, drag, and pressure distributions have been obtained for each wing using a combined experimental and Computational Fluid Dynamics (CFD) approach. Static wing deflections have been measured during wind tunnel tests with Angle of Attack (AoA) ranging from -4° to 14° in 2° increments and wind speeds of 20, 30, and 40 mph. These deflections have been used to calculate the forces and pressure distributions on the Nighthawk during the respective flight conditions.

1.3 Measuring Pitch Performance

There are three primary methods for studying aircraft performance. They are experimental measurements (usually performed in a wind tunnel), computational analysis, and flight testing. Experimental and computational methods are discussed here.

1.3.1 Experimental Approaches. Wind tunnel measurements often include force and moment data such as lift, drag, pitching moment, and roll moment. This data is obtained using a highly sensitive balance, which holds the wind tunnel model in place. The model transfers forces to the balance, which causes the balance to bend slightly. The deformation in the balance is measured using extremely sensitive strain gauges. This deformation is then used to resolve the axial and normal forces on the balance. A transformation matrix is used to transform the forces on the balance into aerodynamic forces and moments on the model [3].

There are many other methods used to examine aerodynamic effects on a body. Pressure transducers can be mounted on the body or pressure sensitive paint can be applied to examine surface pressure. Smoke seeding can be used to examine streamlines. Hot wire anemometers or laser velocimetery can be used to measure the speed

of the flow. Oilflow and tufts can be used to examine the flow on the surface of the body [3].

A great deal of information can be obtained using these experimental methods. When properly applied, these methods provide undisputed measurements of physical occurrences. However, each of these methods requires extensive setup and, in some cases, clean up after the tests. As a result, time constraints and budget limitations limit the number of achievable experiments. In addition, some methods, like oilflow, pressure sensitive paint, and wing tufts, may alter the nature of the flow around the body, degrading the accuracy of the results. Most large aerodynamic problems are studied using a combination of computational and experimental methods, leveraging the advantages of both.

1.3.2 Computational Aeroelastic Approaches. The field of aeroelasticity is concerned with the effect of aerodynamic forces on elastic bodies. Dynamic aeroelasticity involves aerodynamic forces, elastic forces, and inertial forces. Static aeroelasticity involves steady state forces. Hence, the inertial forces are neglected in static aeroelastic analysis and only the aerodynamic and elastic forces are considered [15]. A static aeroelastic analysis does not require knowledge of the mass properties of the elastic body.

There are three approaches to solving aeroelastic problems [20]: fully coupled, closely coupled, and loosely coupled. The fully coupled approach involves combining and simultaneously solving the fluid, structure, and moving grid problems as one large system. The closely coupled approach solves the fluid and structure problems separately, but passes loads and deflections between the two. The loosely coupled approach is similar to the closely coupled approach, but delays passing loads and deflections until the fluid solution has reached steady state.

A significant advantage of using a computational approach is the extent of flow data obtained. Flow features such as separation bubbles and vortices can be analyzed extensively using iso-surfaces, images of streamlines, and vector plots. The effects of

these features can be understood using pressure contour plots. Force and moment data can be obtained for individual parts of the aircraft like the wing or the tail or for the entire aircraft. These solutions are relatively inexpensive to obtain.

As impressive as they are, CFD solutions are still an approximation of physical phenomena. These solutions can provide great insight into flow features, but they must be approached with a healthy degree of skepticism. The solvers and models that are used need to be tested and validated. Appropriate input parameters are required for accurate results. Solutions should be scrutinized for non-physical occurrences to ensure the solver was applied appropriately. When possible, CFD solutions should be compared with experimental results.

1.4 Selected Approach

The method of study pursued here combines experimental measurement and CFD. Rather than using a Finite Element Model (FEM) to solve for the deflection in the wing, the deflection of the wing was measured directly using photogrammetry during wind tunnel tests. Obtaining measurements of wing deflection is the first step in analyzing the aeroelastic behavior of the wing. The data collected could also be used in a follow-on study to tune a FEM.

Once the true wing shapes were determined, CFD calculations were performed using the actual wing shapes. These calculations yielded pressure distributions that were used to determine stability coefficients, the drag polar, and the lifting line of the wing.

A significant advantage of the combined experimental and computational approach is the abundance of flow data obtained through CFD. It is relatively simple to analyze the flow during post processing of CFD verses experimental flow analysis methods like pressure sensitive paint and smoke seeding.

1.5 Document Organization

Chapter 2 discusses aerodynamic issues related to flexible wing mini-UAVs. Chapter 3 describes the process of measuring wing deflection using photogrammetry. Chapter 4 details the process used to build and transform the CFD grids and obtain CFD solutions. Results and analysis are presented in Chapter 5 and conclusions are given in Chapter 6.

II. Background and Theory

This chapter addresses the significant aerodynamic issues related to the study of the Nighthawk mini-UAV. In particular, flexible wings, thin airfoils and flight at low Reynolds number are discussed. Previous research in these areas is also mentioned. A basic understanding of these concepts is required to appreciate the analysis of results presented in Chapter V.

2.1 Nighthawk Description

The Nighthawk mini-UAV has been developed by Applied Research Associates, Inc. (ARA) under the direction of the Air Force Research Laboratory (AFRL) for use as an aerial battlefield camera system. It is 20 inches long with a 26 inch wingspan. The center of gravity is located 6.45 inches back from the nose and 2.18 inches up from the base. It carries a forward facing camera, a side facing camera, and a side facing thermal imager. It weighs 1.5 pounds and flies at wind speeds of 18–40 knots (20–46 mph). It exploits GPS and autopilot technology for navigation. It has a loiter time of 70–90 minutes and a range of 2–10 km [1]. Figure 2.1 illustrates the geometric properties of the Nighthawk.

The Nighthawk's body is composed of a carbon-fiber composite. The leading edge of the wing and the wing ribs are also made of carbon-fiber, while the gaps between the ribs are spanned by nylon cloth. The root chord is 6 inches and the wing has an elliptic planform. The root camber of the undeflected wing is approximately 7.8%. The incidence angle is approximately 4.8° and the dihedral of the undeflected wing is approximately 4.9°. The planform area of the wing is 0.0457 m^2 and the Aspect Ratio (AR) is 9.55. Typical Reynolds numbers range from 90,000 to 180,000.

2.2 Previous Research

Several previous studies have focused on flexible wing micro UAVs. These studies provide valuable insight into the behavior of flexible wings and the challenges of low Reynolds number flight. Some results of these studies are presented here.

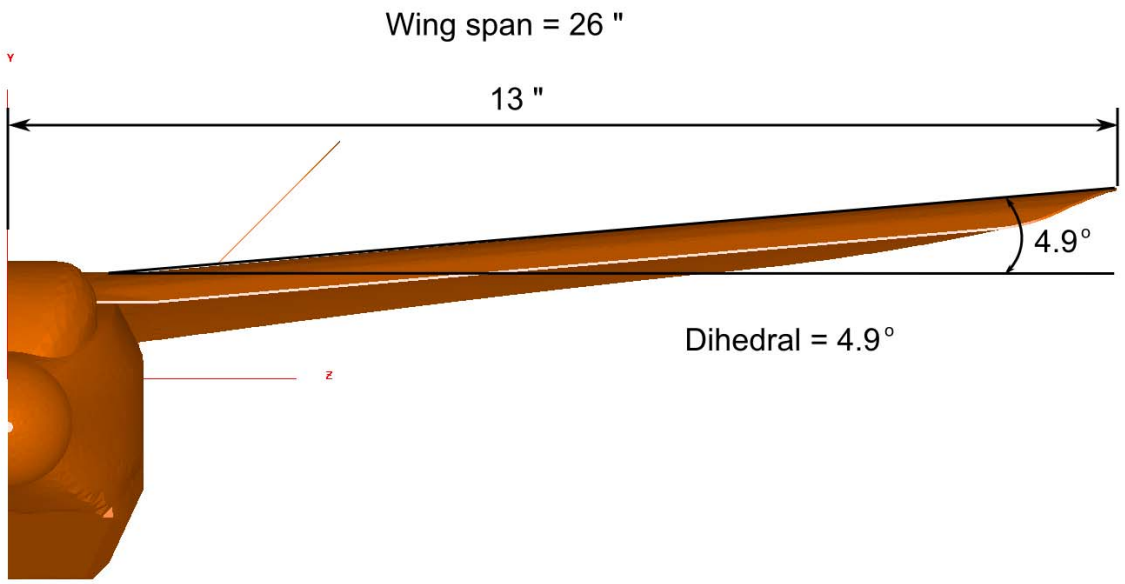

(a) Front view.

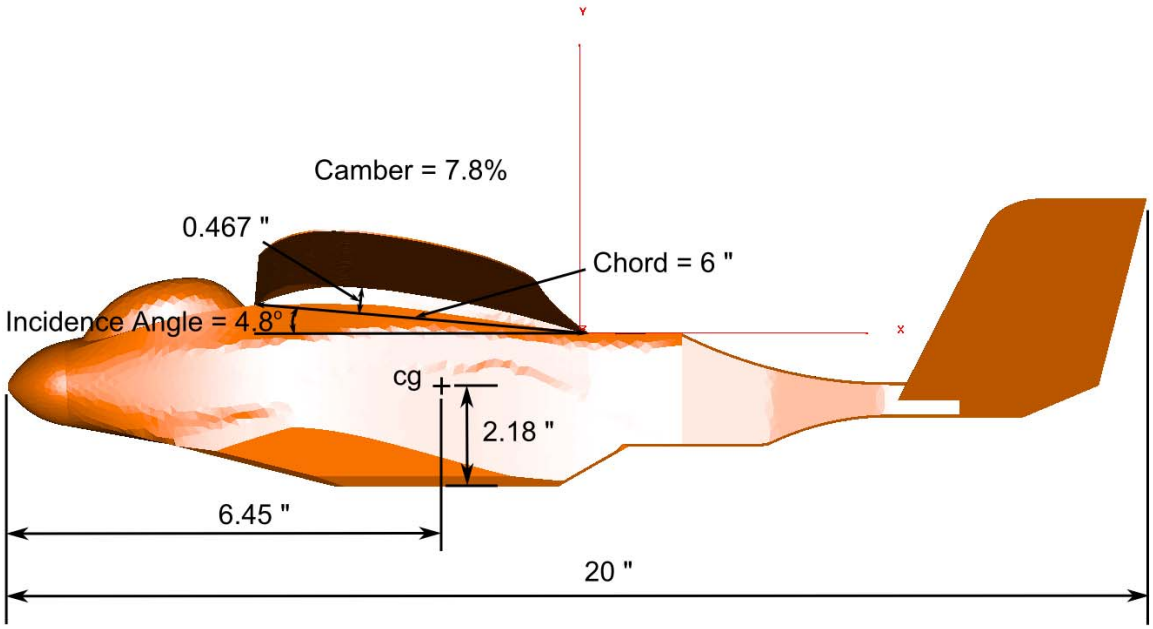

(b) Side view.

Figure 2.1: Geometric properties of the Nighthawk.

DeLuca performed wind tunnel tests on the original BATCAM with a flexible reflex wing made of carbon-fiber and nylon webbing. He compared the performance of the flexible wing with a similar-shaped rigid carbon-fiber wing [10, 11]. This investigation revealed several advantages of the flexible wing over its rigid wing counterpart. These advantages include increased stability in roll, pitch, and yaw, improved efficiency in the form of a higher lift to drag ratio, and improved portability. DeLuca also found that washout in the flexible wing can delay the onset of stall.

Stults performed a closely-coupled aeroelastic analysis of the same UAV [34]. He experimentally determined the mode shapes of the flexible wing. These mode shapes were used to update the grid shape during CFD calculations. Stults found that adaptive washout did not improve the gust response of the BATCAM. However, the flexible wing provided greater stall resistance.

Shyy et al. and Ifju et al. have performed several studies on flexible low Reynolds number airfoils [19, 28–30]. They studied wings with low aspect ratios at Reynolds numbers between 50,000 and 100,000. These studies were focused specifically on improving wing performance for micro air vehicles. They found that wing performance degrades at low Reynolds numbers. They also found that flexible airfoils provide greater stall resistance and improved gust response due to adaptive washout of the wing. The flexible wings had latex membranes. As suggested by Stults, the latex membrane used by Shyy et al. may be the reason that they saw improved gust response while Stults did not [34].

Albertani et al. measured wing deflections for a flexible wing micro air vehicle using visual image correlation [2]. Visual image correlation involves speckle-painting an object with a random pattern and capturing images of the object in a deflected and undeflected state. Deflections are measured by comparing image correlations. They found significant billowing, bending, and washout in the flexible wing. Measured wing displacements can be extremely valuable in computational analysis. For this reason,

experiments that include photographic measurement of wing deflection are becoming more common.

Stanford et al. combined wind tunnel tests with CFD to investigate the deflection of a membrane wing [33]. They performed wind tunnel tests to determine the loads and out-of-plane deflections on a flexible wing micro air vehicle. The deflections were also measured using visual image correlation. They computed pressure fields over an undeformed wing. They then computed the first iteration of the fluid structure interaction to calculate the deflection of the wing. The calculated deflection correlated well with the deflection measured from visual image correlation. This work is a fine example of combining experimental and computational approaches.

Simpson et al. demonstrated the use of photogrammetry during wind tunnel testing to measure wing deflection [31]. The wing they investigated was a warping inflatable wing used for a small UAV. Photogrammetry is the process of measuring the geometric properties of an object using photographs. Given the camera locations, orientations, and a reference length between two points in the photos, the three-dimensional (3-D) locations of points that are common among the photos can be triangulated.

2.3 Flexible Wing Mini-UAVs

Flexible wings offer several advantages over rigid wings. Smoother flight and greater stall resistance at high AoAs are both products of adaptive washout [19]. Adaptive washout occurs when a flexible wing deforms due to the aerodynamic loads experienced during flight. At high AoAs or increased airspeed, the wing will decamber and twist forward reducing the apparent AoA at the wing tip. This provides increased stall resistance and improved gust response.

To illustrate how adaptive washout improves gust response, imagine that a mini-UAV encounters an upward gust during steady flight. The gust briefly increases the effective AoA and the dynamic pressure. As a result, the wing twists forward and

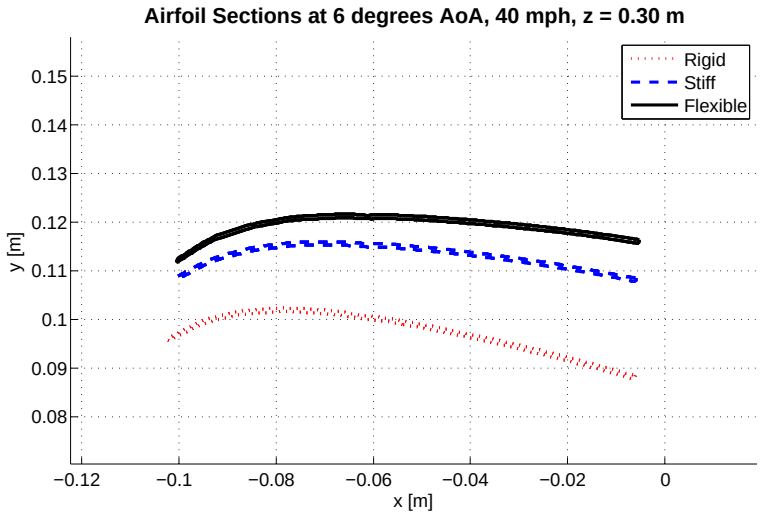

Figure 2.2: Airfoil Sections at 6° AoA, 40 mph, 0.30 m span-wise location illustrate the decambering and forward twist experienced during wingtip washout.

decambers slightly (adaptive washout). The adaptive washout results in slightly less lift, compensating for the increase in lift from the upward gust. The same argument could be made if the aircraft experienced a head-on gust [19].

2.3.1 Roll Stability. Another advantage of a flexible wing is increased roll stability. Dihedral is the span-wise angle of the wing with respect to horizontal. Positive dihedral provides roll stability. As an aircraft experiences a roll disturbance, it enters a sideslip. If the aircraft has dihedral, this sideslip causes an increase in effective AoA for the lowered wing. The result is greater lift on the lowered wing tending to roll the aircraft back towards wings level [23, 27]. The wing tips of a flexible wing aircraft will deflect upwards during flight due to the lift on the wings. This wing deflection increases dihedral and results in greater roll stability.

Another contributor to roll stability is high wing location on the fuselage. As the aircraft enters a sideslip, the air flow is deflected up and over the fuselage increasing the effective AoA on the lowered wing and decreasing the effective AoA on the raised wing. A restoring moment is created, tending to roll the aircraft back towards wings

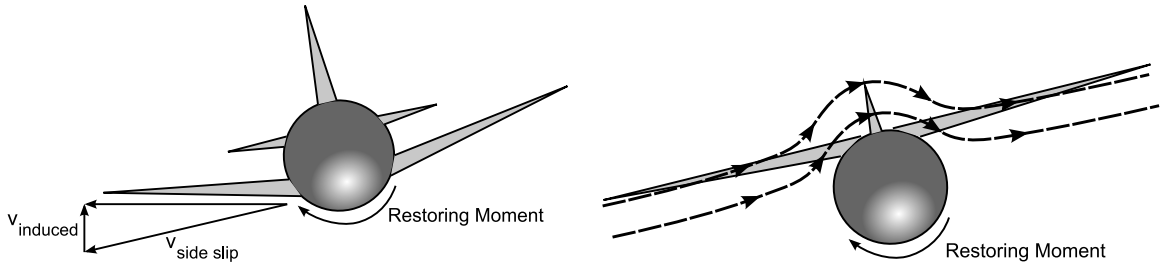

(a) Dihedral contribution.

(b) Fuselage contribution.

Figure 2.3: Roll Stability [23].

level. Figure 2.3 provides a visual representation of how dihedral and high wing mounting contribute to roll stability.

The undeflected wing of the Nighthawk has approximately 4.9° dihedral. It is also mounted on the top of the aircraft. The wing is flexible and experiences up to 2 inches of deflection at the wing tips during flight, which increases the dihedral beyond the nominal 4.9°. All of these factors contribute to favorable roll stability in the Nighthawk.

2.4 Low Reynolds Number Flow over a Thin Wing

Mini-UAVs operate in a low Reynolds number environment (typically less than 200,000). There are several challenges associated with low Reynolds number flight, including laminar flow separation and hysteresis of lift and drag with AoA due to the laminar separation bubble [28, 29]. In addition, there are large fluctuations of AoA and Reynolds number during flight because typical wind gusts are significant compared with flight speeds of 20 to 40 mph.

Low Reynolds number flow over thin airfoils is characterized by laminar flow around the leading edge. Just downstream of the leading edge the flow experiences an adverse pressure gradient. If the laminar flow does not have enough energy to remain attached, it separates. The separated flow forms a free shear layer. Instabilities in the free shear layer are magnified by the adverse pressure gradient and the flow

quickly transitions to turbulent. The turbulent flow transports higher energy fluid down towards the surface of the airfoil. The higher energy flow near the surface may cause the flow to reattach with a turbulent boundary layer. Thus a laminar separation bubble is formed [9, 12, 22, 28].

There are several possible outcomes after laminar flow encounters the leading edge of a thin airfoil. A laminar separation bubble could form as described above. This bubble could either be a short separation bubble where the flow reattaches shortly after separating (see Figure 2.4 (a)), or a long separation bubble where the flow reattaches closer to the trailing edge of the airfoil (see Figure 2.4 (b)). A short laminar separation bubble usually occurs at a higher Reynolds number than a long separation bubble, but not so high as to induce turbulence before laminar separation. A long separation bubble could be as long as 30% of the chord. After the flow reattaches, it could either remain attached with a turbulent boundary layer, or it could separate before reaching the trailing edge (see Figure 2.4 (c)). At high AoAs the turbulent shear layer is unable to reattach to the surface and the result is leading edge stall (see Figure 2.4 (d)). If the boundary layer transitions to a turbulent state before laminar separation occurs, it is more likely to remain attached through the adverse pressure gradient. As the AoA is increased, the turbulent boundary layer may separate near the trailing edge of the airfoil. The separation point will move upstream as the AoA is increased further. This phenomenon is referred to as rear stall.

2.4.1 The Effects of Laminar Separation. Just as there are several possible outcomes for low Reynolds number flow (i.e. short laminar separation bubble, long laminar separation bubble, leading edge stall, or rear stall), each possibility affects the airfoil performance in a different way. The most devastating outcome in terms of airfoil performance is stall. If the airfoil stalls, the lift is greatly reduced and the drag is greatly increased. The events leading up to stall are also important, however. At low Reynolds numbers, a long laminar separation bubble forms and the lift curve is

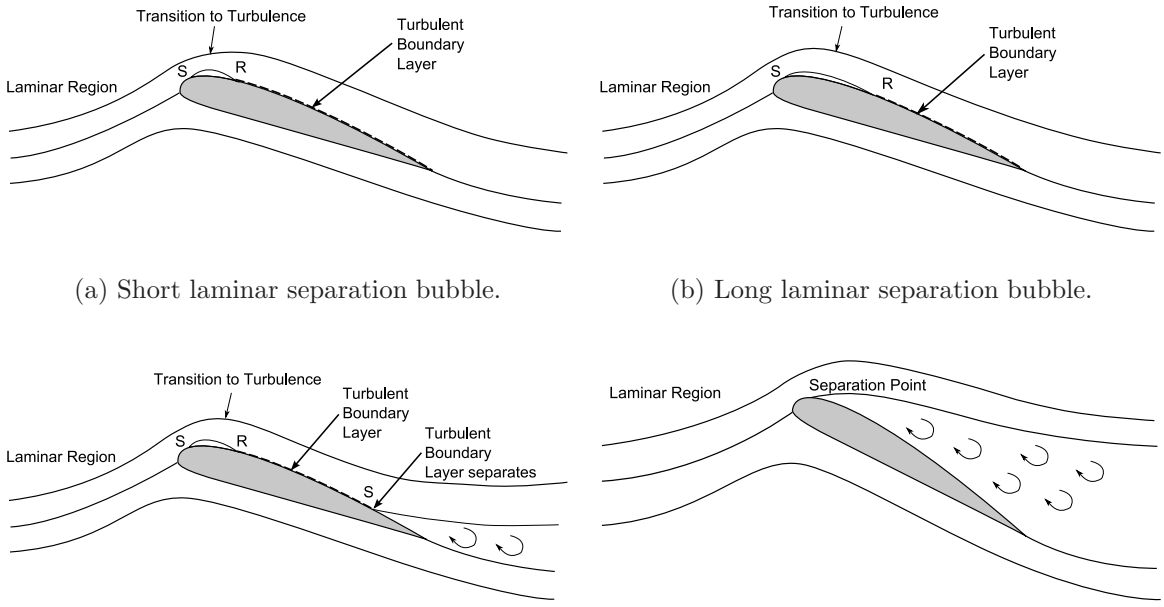

(a) Short laminar separation bubble.

(b) Long laminar separation bubble.

(c) Laminar separation bubble followed by turbulent separation.

(d) Fully Separated.

Figure 2.4: Low Reynolds Number Flow [9, 22].

bent downward. This is referred to as thin airfoil stall and is depicted in Figure 2.5, where C_L is the non-dimensional lift coefficient (defined in Section 2.5) and α is the AoA. The $C_{L\ max}$ is lowest in this form of stall. If the Reynolds numbers are slightly higher and a short laminar separation bubble forms, the lift curve is not affected until higher AoAs are reached. However, once a critical AoA is reached, an abrupt decrease in lift is experienced. This is referred to as leading edge stall in Figure 2.5. If the boundary layer becomes turbulent before a laminar separation bubble can form, the airfoil will experience rear stall (see Figure 2.5) [9]. Of all the stall mechanisms, rear stall is the most favorable because it generally results in the greatest $C_{L\ max}$ and is less prone to hysteresis in the lift curve. Carmichael emphasized the importance of the laminar separation bubble for flow with Reynolds numbers ranging from 70,000 to 200,000 by stating [8]:

> "The laminar separation bubble is still a significant potential performance robber in this region of flight."

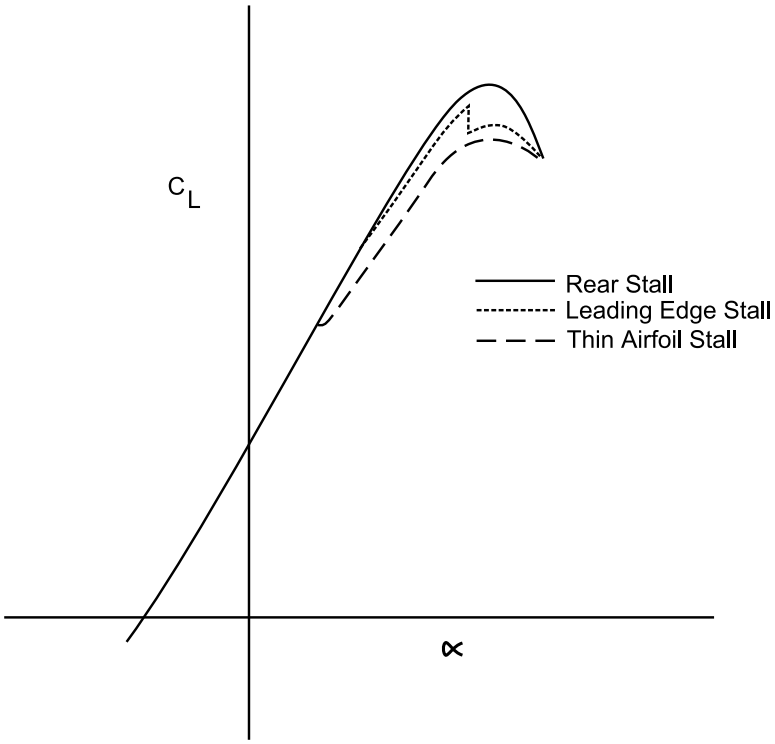

Figure 2.5: Effects of stall mechanism on the lift curve [9].

Figure 2.6 (a) portrays the effects of hysteresis in the lift and drag curves due to a short laminar separation bubble and leading edge stall [22]. The lift curve maintains its typical shape until a critical AoA is reached at which point a sudden drop in lift is experienced. Decreasing the AoA slightly will not restore the lift. To restore the lift, the AoA must be decreased significantly and then increased to some value below the critical AoA. Drag is also affected negatively once the critical AoA is reached. Figure 2.6 (b) shows a hysteresis loop for a long laminar separation bubble. In this case the lift and drag are poor as AoA is increased to the critical AoA. However, once the critical AoA is reached, the lift and drag performance improve as AoA is decreased. In Figure 2.6, C_L is the lift coefficient, C_D is the drag coefficient (defined in Section 2.5), and α is the AoA.

A technique that has been successfully applied to avoid laminar separation bubbles is the use boundary layer trips, which cause a disturbance in the flow and cause the boundary layer to become turbulent earlier than it would otherwise. Turbulent

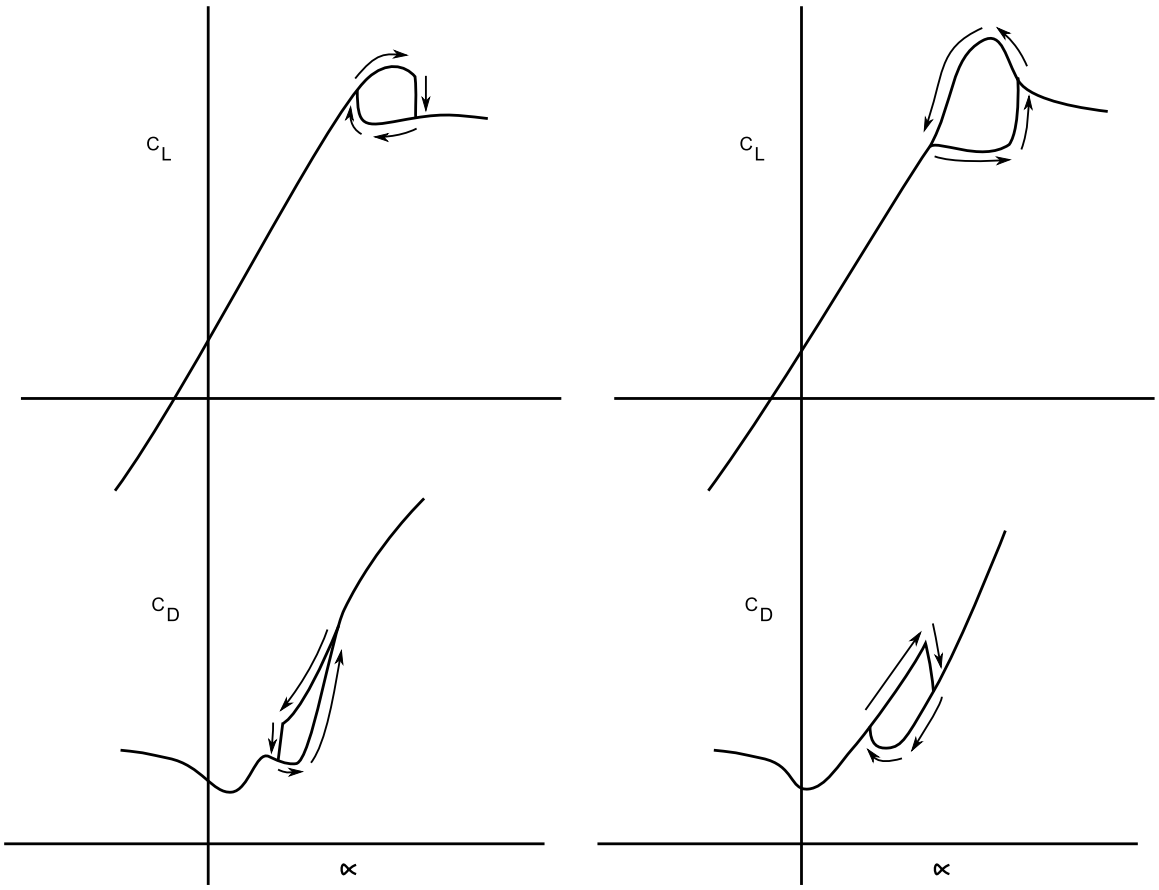

(a) Short laminar separation bubble.

(b) Long laminar separation bubble.

Figure 2.6: Lift and Drag Hysteresis [8, 22].

boundary layers pull high energy flow from the freestream closer to the wall. This allows the flow to stay attached through the adverse pressure gradient. Wire, tape, or even increasing surface roughness with sand paper are ways to trip the boundary layer to turbulent. Turbulent boundary layers grow much faster than laminar boundary layers and the skin friction drag for a turbulent boundary layer is higher than for a laminar boundary layer. However, the turbulent viscous drag is a small price to pay to avoid laminar separation.

2.5 Wing Efficiency

Non-dimensional parameters are often used to facilitate comparisons of lifting bodies over various flight regimes. The most common non-dimensional parameters are the lift and drag coefficients. The lift coefficient, C_L, is defined by,

$$C_L = \frac{L}{\frac{1}{2}\rho_\infty v_\infty^2 S} \tag{2.1}$$

where, L is the lift force, ρ_∞ is the freestream density, v_∞ is the freestream velocity, and S is the reference area (usually the wing planform area). Similarly the drag coefficient, C_D, is given by,

$$C_D = \frac{D}{\frac{1}{2}\rho_\infty v_\infty^2 S} \tag{2.2}$$

where, D is the drag force. The ratio of the two gives the lift-to-drag ratio, which is a measure of the performance of the wing.

2.5.1 Lift. Thin airfoil theory can be used to predict the performance of a wing in terms of lift and drag. The basic assumptions used in thin airfoil theory include:

- The flow around the airfoil is inviscid.
- The angle of attack is small.
- The influence of airfoil thickness on pressure forces is small.

Using these assumptions, it can be shown that the theoretical value of the lift coefficient is given by [5]:

$$C_L = 2\pi\alpha \tag{2.3}$$

where C_L is the lift coefficient and α is the AoA in radians. For a cambered airfoil, the lift curve is shifted up so that the lift at 0° AoA is positive.

A wing of finite AR will have a lift curve with a lower slope than the theoretical lift curve. The correction for AR is given by [5]:

$$C_{L\ \alpha} = \frac{C_{l\ \alpha}}{1 + \frac{57.3 C_{l\ \alpha}}{\pi e (AR)}} \tag{2.4}$$

where $C_{L\ \alpha}$ is the lift curve slope corrected for AR (in $\frac{1}{\text{deg}}$), $C_{l\ \alpha}$ is the theoretical lift curve slope of a 2-D airfoil ($C_{l\ \alpha} = 0.10966\ \frac{1}{\text{deg}}$), and e is Oswald's wing efficiency factor. The wing efficiency factor typically ranges from 0.6 to 0.95. An elliptical wing usually has a high wing efficiency factor.

2.5.2 Drag. There are three main sources of drag—parasite drag, C_{D0} (drag at zero lift), induced drag, C_{Dind} (drag due to lift), and wave drag, C_{DM} (drag due to compressibility effects). The parasite drag includes skin friction and form drag. The induced drag is given as a function of lift, $C_{Dind} = \frac{C_L^2}{\pi e (AR)}$ so that [5],

$$C_D = C_{D0} + \frac{C_L^2}{\pi e (AR)} + C_{DM} \tag{2.5}$$

At low Mach numbers the wave drag is negligible. In the low Reynolds number, low Mach number flight regime, induced drag is the most significant source of drag.

2.5.3 Lift-to-Drag Ratio. As mentioned previously, wing efficiency is often measured in terms of the lift-to-drag ratio, $\frac{L}{D}$. For a propeller aircraft, the most efficient cruise (best range) is at $(\frac{L}{D})_{max}$ while the best loiter is at $0.866(\frac{L}{D})_{max}$ [27].

In the case of the Nighthawk, optimization for best loiter is most beneficial since that will allow the most time on target.

In light of the information presented in this chapter, the following parameters are important to consider when comparing the performance of the flexible, stiff, and rigid wings: lift-to-drag ratio, stall angle, and maximum lift coefficient. The roll stability and gust response are also important factors to consider.

III. Experimental Methods—Determining Static Wing Deflection

The focus of the experimental effort was to measure the static wing deflection for various AoAs and wind speeds. The deflection was obtained for the flexible wing and the stiff wing. Since the focus of the experimental effort was to obtain wing deflections, force data was not obtained during wind tunnel testing. The AoAs of interest ranged from -4° to 14° in increments of 2° and the velocities of interest were 20, 30, and 40 mph. The AoA was measured relative to the body axis of the Nighthawk (parallel to the base and through the nose). Tables A.1 and A.2 list the recorded AoAs and wind speeds for test cases for the flexible wing and stiff wing, respectively.

Photogrammetry is the process of measuring the geometric properties of an object based on images of the object [21]. Modern photogrammetry is used to obtain 3-D measurements of objects using photos from various angles. If sequences of photos are captured simultaneously, the 3-D motion of an object can be obtained. Photogrammetry is an ideal tool for measuring wing deflections because it does not disturb the flow over the wing and 3-D deflections over the entire wing can be measured simultaneously. The deflection obtained via photogrammetry was used to adjust the shape of the aerodynamic grid for CFD solutions, a process which will be discussed in Chapter IV. The following references give some excellent information on photogrammetry: [6, 14, 21, 24, 36].

3.1 Nighthawk Preparation

A production model Nighthawk was provided by Applied Research Associates (ARA) for wind tunnel testing. The model had no internal components other than the motor for the propeller, which the nose spinner was mounted on. Both the flexible and the stiff wings were also provided by ARA. Three significant changes were made to the Nighthawk before testing began. The Nighthawk was fitted with an internal mounting block, the upper wing surface was marked with high contrast targets for

(a) Adding the sting.

(b) Sliding on the pod cover.

(c) With the wing secured.

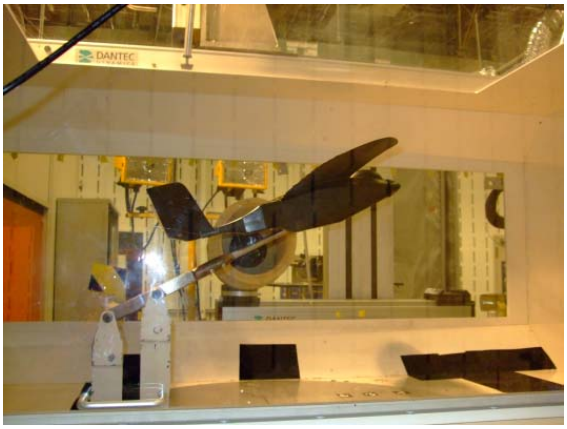

(d) Mounted in the wind tunnel.

Figure 3.1: Mounting the Nighthawk in the wind tunnel.

photogrammetry, and the propeller blades were removed to compare more closely with the CFD model. The ruddervators were free throughout all tests.

The Nighthawk was fitted with an internal mounting block that was built using stereolithography. The mounting block was made to fit inside the removable camera pod. It was secured to the Nighthawk with 4 machine screws and a sting was attached to the mounting block with 3 machine screws. A hole was drilled in the pod cover to accommodate the sting. Figure 3.1 illustrates the process of fitting the Nighthawk with a mounting block and sting.

The upper wing surface was marked with high contrast targets (see Figure 3.2). These targets acted as reference points for measuring the deflection of the wing. Two types of targets were used on the upper wing surface—non-coded targets (circular dots) and coded targets (circular dots surrounded by banded sections). The non-coded targets were bright yellow circular stickers with diameters of $\frac{1}{4}$ inch. This size was selected to ensure the diameters were at least 8-10 pixels in photographs, which is ideal for target recognition during image processing. The coded targets are recognized by PhotoModeler® and are used to automatically orient the photos during post processing.

Coded targets were printed on high gloss photo paper and secured to the wings and upper surface of the Nighthawk using double-sided tape. The non-coded targets were glued to the upper surface of the wing using Super Glue®. The targets were positioned on the wing in rows spaced approximately 1 inch apart with the first row starting $\frac{1}{2}$ inch behind the leading edge. This spacing ensured easy sorting of the targets during post processing. Figure 3.2 shows the Nighthawk after it was marked with targets.

3.2 Wind Tunnel Description

Testing was conducted in the low speed open circuit wind tunnel at the Air Force Institute of Technology (AFIT). The intake section is 131 inches wide by 108 inches high. There are four anti-turbulence screens and an aluminum honeycomb flow straightener. DeLuca measured a freestream turbulence of 2.25% in the AFIT wind tunnel [10]. The the test section is 44 inches wide, 31 inches high, and 72 inches long. Maximum airspeed in the test section is 150 mph. There is a window on the ceiling and on each side of the test section. There is a 25 ft diverging section between the test section and the fan. The wind tunnel is driven by a fan with a 220 BHP electric motor. The wind tunnel exhausts above the fan [17]. Figure 3.3 is a schematic of the AFIT low speed wind tunnel.

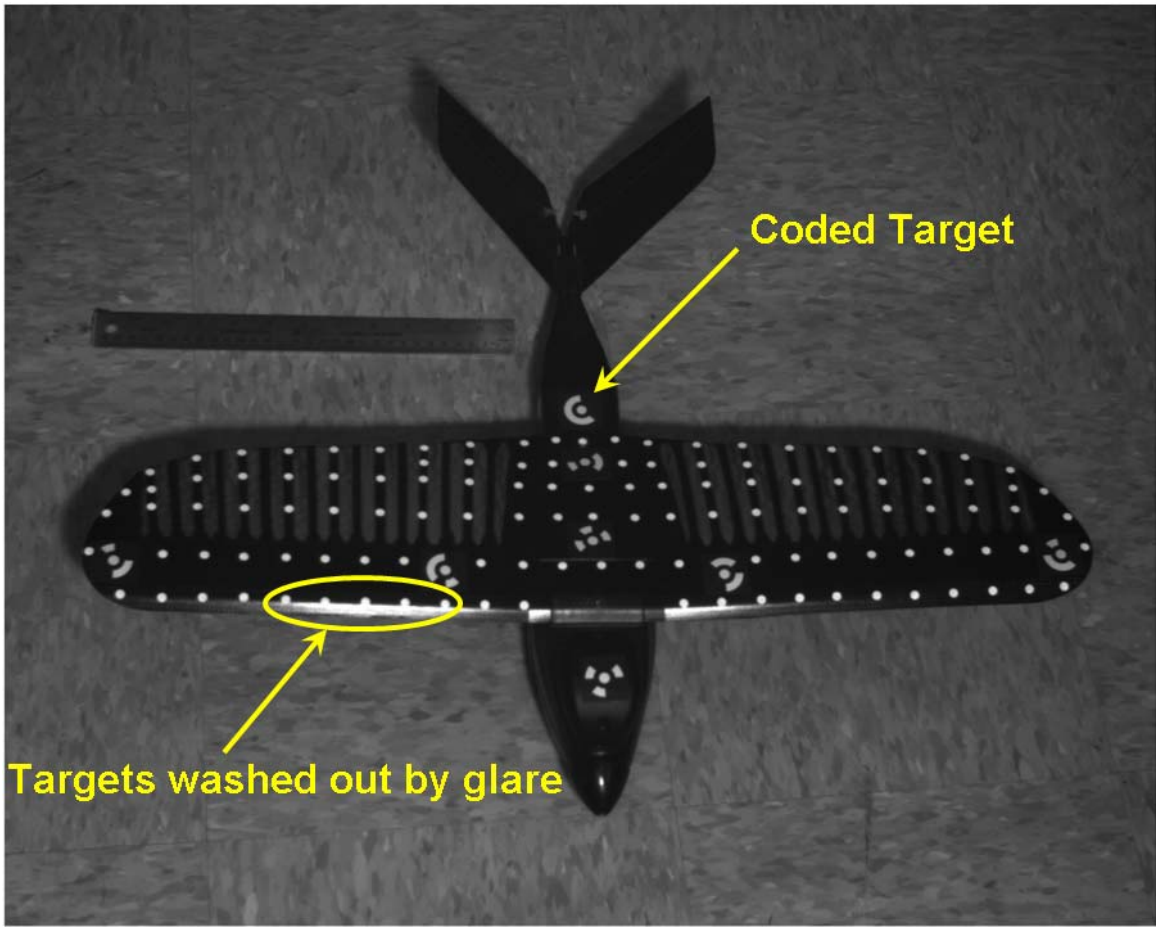

Figure 3.2: Nighthawk mini-UAV marked with reflective targets.

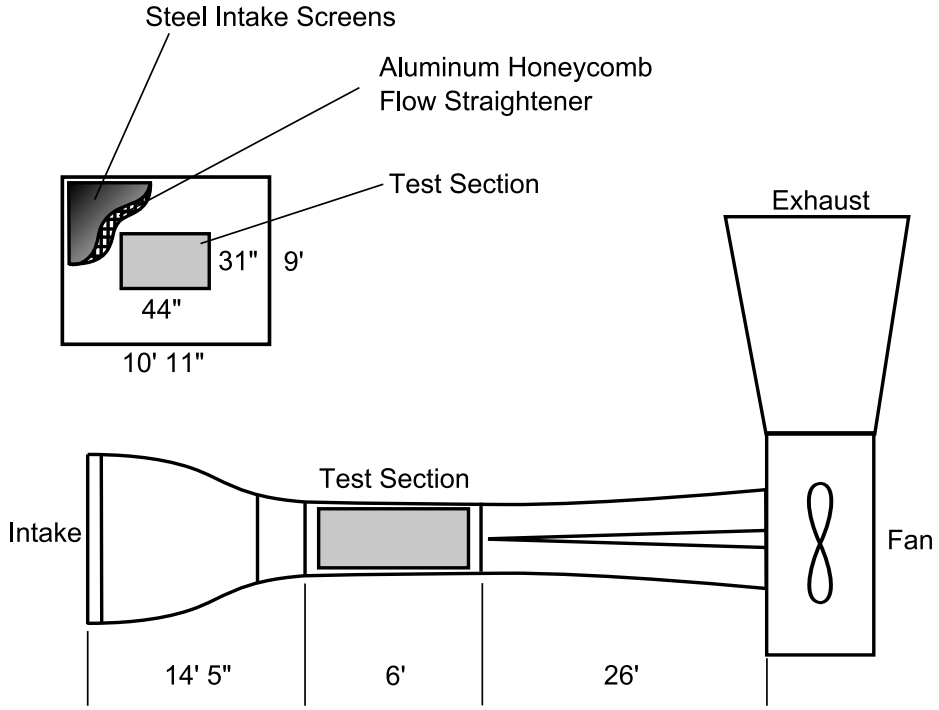

Figure 3.3: AFIT wind tunnel schematic. Adapted from DeLuca [10] and Gamble [17].

3.3 Wind Tunnel Preparation

The wind tunnel has a white floor, which contrasts well with the black wing of the Nighthawk. However, at moderate speeds and AoAs, washout occurs and the targets near the leading edge of the wing blend into the wind tunnel floor when viewed from above. To provide contrast for the targets on the leading edge, black felt was attached to the floor of the wind tunnel. This action ensured target recognition despite washout. Figure 3.4 shows pictures of the wing during wind tunnel testing. It demonstrates the views each camera had of the Nighthawk. Notice the felt in image 3.4 (c) prevents the leading row of dots from blending into the wind tunnel floor. Similarly, the felt in image 3.4 (a) prevents the trailing targets from blending into the floor.

Six coded targets were secured to the wind tunnel floor to act as reference points during post processing. These targets were visible in each camera. Targets 1 and 2 define the z-axis (positive from 2 to 1). These targets also define the scaling factor

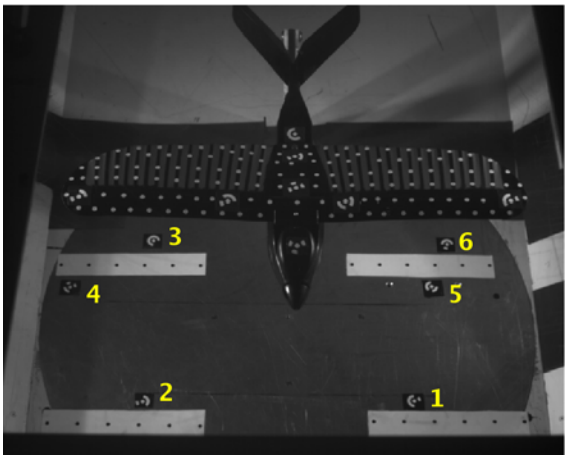

(a) View from Camera 1.

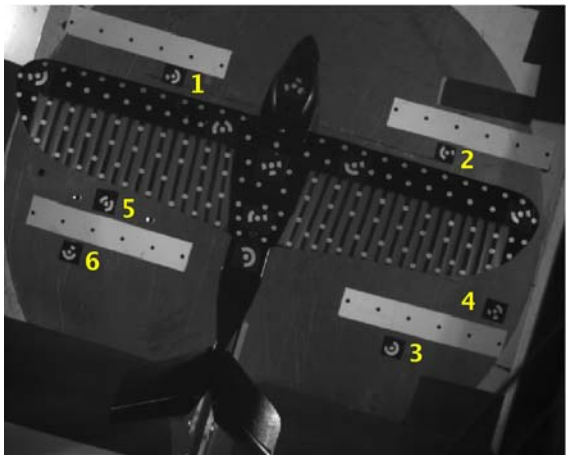

(b) View from Camera 2.

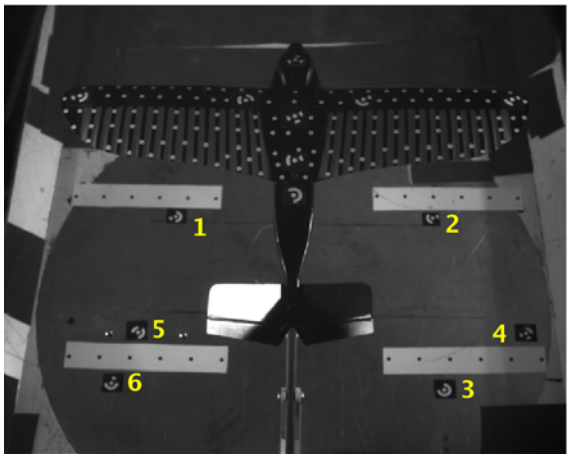

(c) View from Camera 3.

Figure 3.4: View from each camera during wind tunnel tests. 0° AoA, 20 mph, flexible wing.

since they are separated by 18.53 inches. Targets 2 and 3 define the x-axis (positive from 2 to 3). The y-axis is normal to the wind tunnel floor (up is positive).

At AoAs less than 4°, the majority of the targets (i.e. the targets on the wing) lie in a plane approximately 15 inches above the wind tunnel floor. The only targets out of this plane were the coded targets used to define the scale and axes. When there is a concentration of points in one plane with only a few out of the plane, the photogrammetry software, PhotoModeler®, performs a calibration that causes residuals for the outliers to increase. As a result, the triangulated positions of the coded targets on the floor were less accurate. Since these targets are used to define the scale and axes, the accuracy of all point locations would be degraded. To counter this effect and maintain accuracy for all points in the project, non-coded targets were added to the wind tunnel floor. This was done by printing black dots on white paper and taping the paper to the floor with double-sided carpet tape. The addition of these targets ensured that PhotoModeler® did not treat the coded targets on the wind tunnel floor as outliers.

3.4 Camera Setup

Three synchronized Basler 501k high speed digital cameras were used to capture image sequences during wind tunnel testing. Each camera is capable of capturing 74 frames per second (fps) at maximum resolution, which is 1280 x 1024 pixels [4]. A Personal Computer (PC) workstation was used to drive the cameras and store images. Each camera was connected to its respective video capture board in the PC. EPIX®image capturing software was used to control the cameras via their respective video capture boards.

Acquiring high quality image sequences required synchronized cameras with proper lighting. Sections 3.4.2 through 3.4.4 give the details of camera setup.

3.4.1 Camera Positioning. To get the best view of the wing, all cameras were positioned atop the wind tunnel and aimed through the viewing glass above the

test section. They were positioned in-line with the flow direction with one in front of the model, one directly above the model, and one trailing the model. There was at least a 30° separation angle between the cameras. The cameras were positioned far enough from the model to allow each camera a full view of the wing. Figure 3.5 shows the position of the cameras atop the wind tunnel. It also illustrates the viewing angle of each camera. Camera 1 is positioned ahead of the Nighthawk, Camera 2 is directly above it, and Camera 3 is behind it.

3.4.2 Synchronization. Since the wing experienced high frequency oscillations in the wind tunnel, it was important to ensure the cameras were synchronized. The first camera was configured as the master and the other two were slaves. The settings for camera synchronization are included in Appendix B.

A test was performed to ensure the cameras were synchronized. It involved marking a fan blade with reflective targets, turning the fan on high, and capturing an image sequence from all three cameras. Black tape was used to mark graduated increments around the outer rim of the fan. This facilitated comparing the location of the reflective targets among images. The Area of Interest (AoI) was reduced to 480 pixels x 480 pixels to increase the available frame rate. The frame rate was adjusted to 156 fps and the exposure time was reduced to 0.2 ms. Since the exposure time was low, the reflective target showed little movement or streaking in the photos. The fan made 2.5 revolutions in 19 frames. At a frame rate of 156 fps, this equates to 20.5 rev/s or 1230 rpm. The image sequence was examined frame-by-frame to verify that the reflective target was in the same relative location in all three images. Figure 3.6 shows an example of a typical image set. It clearly shows that the cameras were synchronized because the bright marks on the fan blade are in the same position in each image.

3.4.3 Lighting. Proper lighting was paramount in capturing high quality images. The lighting was required to illuminate the reflective targets on the wing without producing glare off the wing, the wind tunnel viewing glass, or the wind

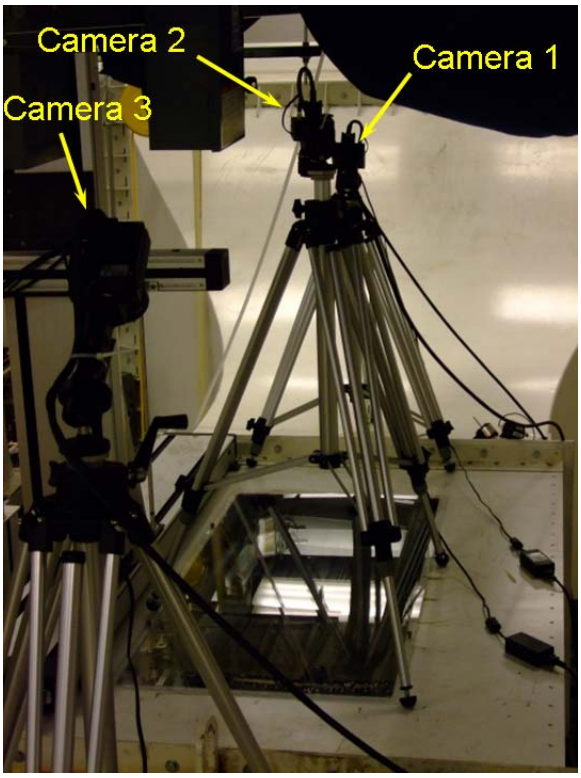

(a) View atop the wind tunnel.

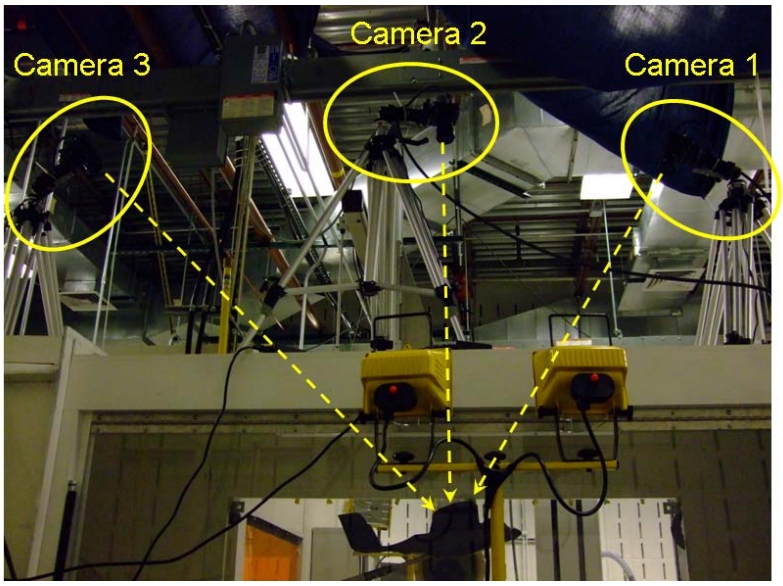

(b) View from the ground.

Figure 3.5: Camera positions atop the wind tunnel.

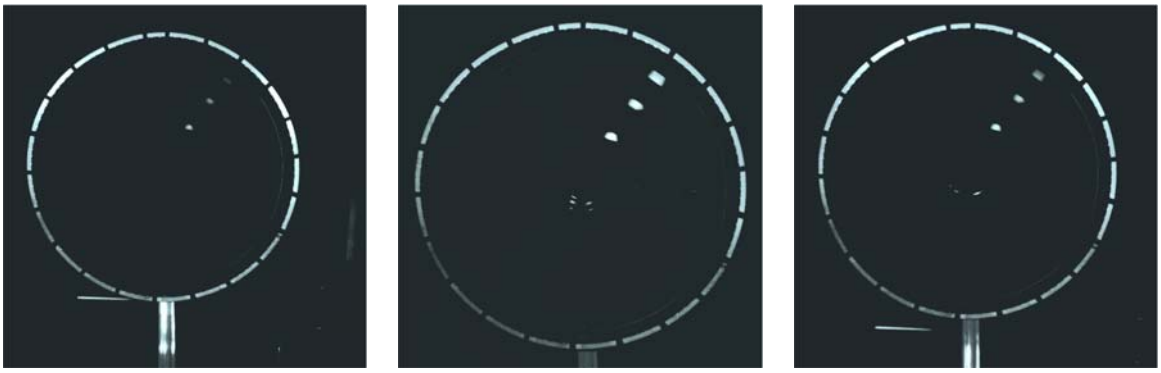

(a) Camera 1. (b) Camera 2. (c) Camera 3.

Figure 3.6: An under-exposed image set of a fan running at 1230 rpm during a synchronization test. Each image displays the fan rim and three reflective marks on the fan blade. This figure demonstrates that the cameras were synchronized.

tunnel floor. A good example of how glare off the wing can obscure targets thereby eliminating the possibility of triangulating their positions can be seen in Figure 3.2. Some targets on the leading edge of the starboard wing are washed out in this image.

Two 1000 W halogen lamps were aimed at the wing through each side window of the wind tunnel. They shone across the top of the wing with enough intensity to illuminate it without creating glare in any of the three cameras. Sheets were hung above the cameras to prevent overhead lights from glaring off the viewing glass and back into the cameras.

3.4.4 Calibration. The purpose of camera calibration is to calculate the focal length, the location of the principal point, the lens distortion, and other camera aberrations that distort collected images. As light travels through a lens, the rays bend and converge to a point. The focal length is the distance from the lens to the point of convergence. The principal point is the point on the focal plane that is directly behind the nodal point of the camera lens. It can be thought of as the alignment of the lens with the center of the focal plane. The principal point is very near the center of the focal plane. Objects near the fringe of an image will slant towards the center (pin cushion effect). This is caused by lens distortion. The focal

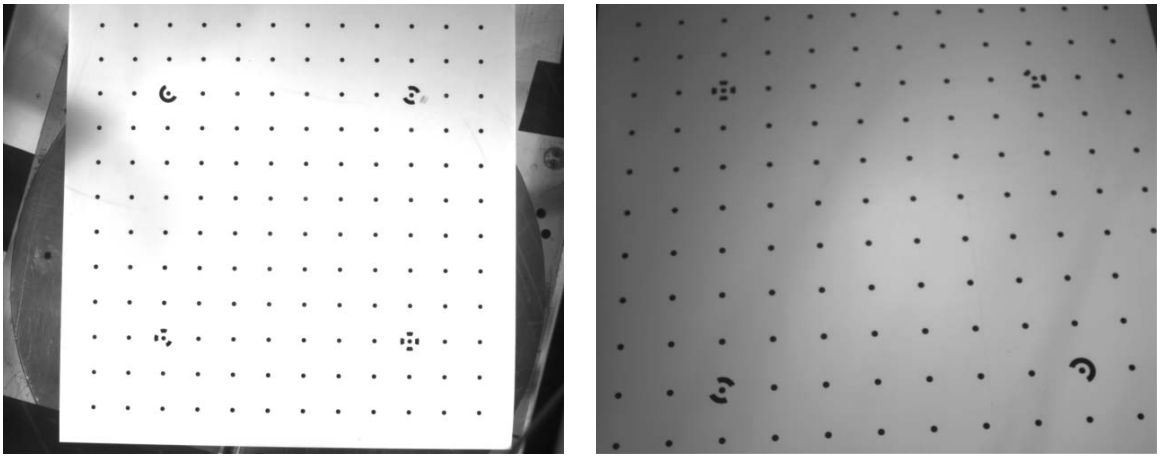

(a) Entire calibration grid.

(b) Image used for calibration. Grid points fill the entire image.

Figure 3.7: Images of the camera calibration grid.

length, principal point location, and lens distortion parameters are used to remove these distortions and improve the accuracy of the photogrammetry calculations [36].

Camera calibration involves taking 12 photos of a square calibration grid that is secured to the floor. The calibration grid consists of 144 targets in a 12 x 12 equally spaced grid. Its dimensions are 3 ft x 3ft. There are 140 non-coded targets and 4 coded targets, which are located at the third station in from each corner along the diagonal. A good calibration photo has a significant portion (at least 80%) of the photo filled by the calibration grid. It is acceptable to have points on the grid extend beyond the bounds of the photo as long as all 4 coded targets are visible. Figure 3.7 shows a picture of the entire calibration grid (a) and a picture that is suitable for camera calibration (b). The 12 calibration photos are taken as follows: one photo is taken from each side of the grid with the camera in the upright position, one from each side with the camera rolled 90° to the right, and one from each side with the camera rolled 90° to the left.

An accuracy test was performed to ensure the wind tunnel glass did not distort the images and decrease measurement accuracy. This test involved capturing image sets of the ARAMIS calibration slate. The ARAMIS calibration slate is a black slate

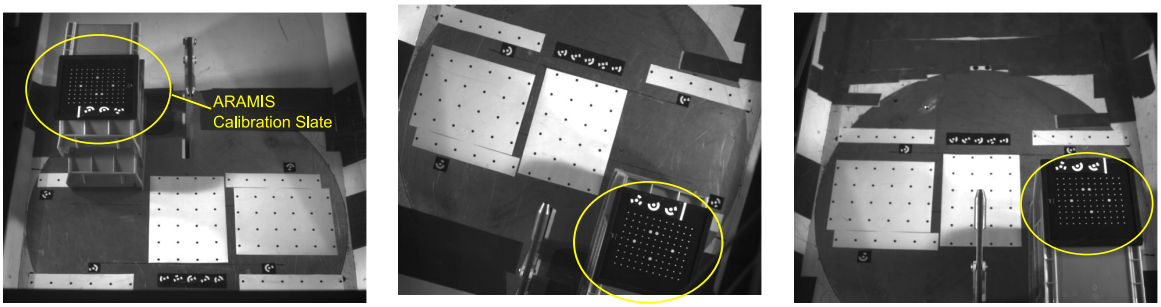

(a) View from Camera 1. (b) View from Camera 2. (c) View from Camera 3.

Figure 3.8: Photo set from an accuracy test using the ARAMIS calibration slate.

with small white dots in a grid measuring 135 mm x 80 mm. It is not typically used for camera calibration. However, because it has precisely located dots, it was useful in a test to determine the accuracy of photogrammetry measurements. It was placed in the wind tunnel at about the same height as the wing. Image sets of the calibration slate were captured. The coded targets on the floor were used to scale the images, and the size of the calibration grid was measured using photogrammetry. Since the calibration slate is smaller than the wing, the test was performed several times with the calibration sheet moved to different positions covering the same field of view occupied by the wing. The maximum error obtained in these accuracy tests was 0.62 mm. This error is acceptable for the current application since actual tip deflection was as much as 2 inches. Figure 3.8 is an image set of the calibration slate used in the accuracy test.

3.5 Wind Tunnel Operation

AoA and wind speed were the independent variables during wind tunnel testing. Yaw angle and roll angle were control variables, held constant at 0°. The model was adjusted to the target AoA using the wind tunnel controller, National Instruments' LabVIEW. The actual AoA of the Nighthawk was confirmed using an inclinometer for each angle tested.

In wind tunnel testing it is common to set the wind speed then perform a sweep of the AoAs while holding the velocity constant. The camera positioning allowed for only a 10° variation in AoA before targets would be lost from view. As a result, the velocities were varied at each AoA rather than performing an AoA sweep for each velocity. The cameras were positioned to accommodate testing for 6° to 14° AoA. Then the cameras were repositioned and tests were conducted for −4° to 4° AoA.

The following test was performed at each AoA. A static image set of the wing was captured before the wind tunnel was turned on. The velocity was increased to 20 mph and held constant for about 30 seconds until transients died out. Image sequences were then captured and the process was repeated for the 30 mph case and the 40 mph case. A second static (no-wind) image set was obtained after the 40 mph test was complete to compare with the first image set and ensure the wing returned to its original location (i.e. the wing or model didn't shift during the test).

3.6 Image Capturing

The cameras were controlled using EPIX® software. Since Camera 1 was set up as the master, all commands were sent to the cameras simultaneously by sending a command through the Camera 1 dialogue. Static images of the Nighthawk were captured by taking snapshots while image sequences were captured by saving image streams to the camera buffers. Image sequences were then downloaded to the PC workstation. This process allowed the cameras to capture sequences at maximum frame rate (up to 74 fps). An image sequence was captured for each of the 60 test cases listed in Tables A.1 and A.2.

For some high speed (30 to 40 mph), negative or 0° AoA cases (listed in Table 3.1) the wing experienced large oscillations. At these conditions, the targets were moving fast enough to make tracking from one frame to the next very difficult. Instead of capturing sequences at the maximum frame rate, the capture rate was tuned to be slightly higher than the natural frequency of the first bending mode. The natural frequency was estimated by adjusting the capture rate until there appeared to be

almost no wing movement in the video. At the lower capture rates, the targets moved very little from one frame to the next and tracking was much easier. There is an alias in the motion of the wing measured by the reduced capture rate, but the amplitude of motion for the wing can still be found by analyzing the aliased measurement through several cycles of motion. Test cases not listed in Table 3.1 experienced less wing motion and were captured at the maximum frame rate (74 fps).

Table 3.1: List of cases run with reduced capture rate.

AoA [deg]	Speed [mph]	Wing Type	Estimated Natural Frequency of 1^{st} Bending Mode [Hz]	Capture Frequency [Hz]
-4	30	Flexible	25.2	25.711
-4	40	Flexible	25.4	25.711
-2	30	Flexible	26.5	27.507
-2	40	Flexible	26.8	27.307
0	40	Flexible	31	31.602
-4	40	Stiff	36	36.545
-2	40	Stiff	36	39.028

3.7 Image Post Processing Using PhotoModeler®

The purpose for capturing these image sequences was to measure the static displacement of each target on the wing. The displacement was measured by comparing the location of each target with no wind (i.e. the undeflected location) to the average deflected location for each wind speed.

A set of three simultaneous images from each camera constitutes an image set. The location of each target on the wing can be triangulated from that image set. This is done using PhotoModeler® software. Processing includes: recognizing the targets in each image, scaling and orienting the photos, tracking targets through each frame, and exporting x, y, z coordinates for target to a data file. A detailed set of instructions for processing in PhotoModeler® is included in Appendix C.

Figure 3.9 shows a processed epoch (or frame) with coded and non-coded targets marked in each of the photos. Coded targets are marked with a circular symbol and

non-coded targets are marked with a cross. Once the first frame has been processed (i.e. the 3-D location of each target has been solved), the targets can be tracked through the remaining frames. The location of each target in each frame can then be exported to a data file. The final result is a set of 3-D target locations in time.

(a) Processed image from Camera 1.

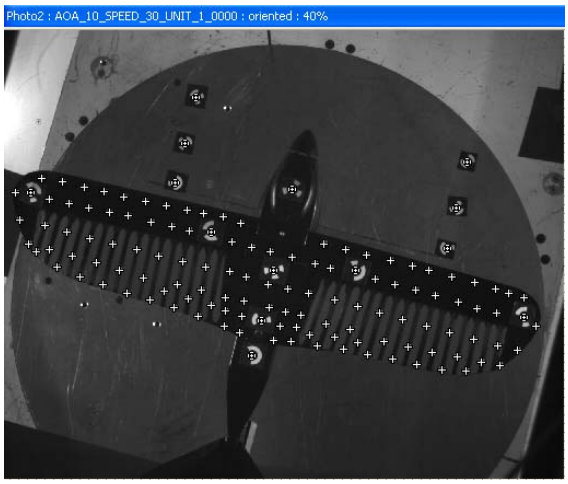

(b) Processed image from Camera 2.

(c) Processed image from Camera 3.

Figure 3.9: Processed images from PhotoModeler®.

IV. Computational Approach

Chapter III described how the location of each target on the wing surface was obtained using photogrammetry. This chapter describes the data processing and CFD approach. The geometry of the Nighthawk was defined in a SolidWorks® model. This geometry was used to create the grid for the undeflected wing shape in Gridgen®. The wing deflection was calculated using a Thin Plate Spline (TPS) method with the point locations measured in Chapter III. The undeformed grids were adjusted to include wing deflections. The 3-D grid was built in SolidMesh. The flow solution was obtained using FLUENT®. Finally, the data was post processed in MATLAB®, FLUENT®, and FieldView. The work flow described here is summarized in Figure 4.1.

4.1 Building and Adjusting Aerodynamic Grids

The original computer aided design (CAD) model was supplied by ARA as a SolidWorks® assembly. The model was simplified by removing the following details:

- Propeller blades.
- On/off switch.
- Counter-sunk screw detail in the GPS unit.
- Leading edge wing clamp.
- Wing button on the trailing edge.

In addition, the nose was smoothly joined to the fuselage and all holes were patched to provide a "water-tight" model. Figure 4.2 shows the Nighthawk model before and after these simplifications. The purpose of these simplifications was to create a smoother grid over the surface of the Nighthawk without compromising the fidelity of the model.

4.2 Building Surface Grids in Gridgen®

After adjustments were made to the original SolidWorks® assembly, the Nighthawk model was exported in Initial Graphics Exchange Specification (IGES) format for fur-

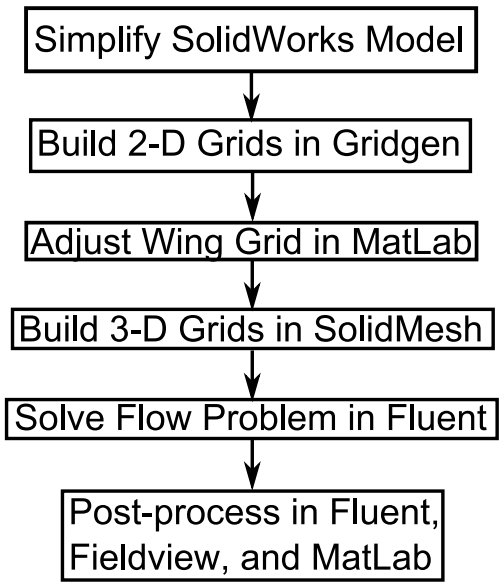

Figure 4.1: Flow chart illustrating the computational approach.

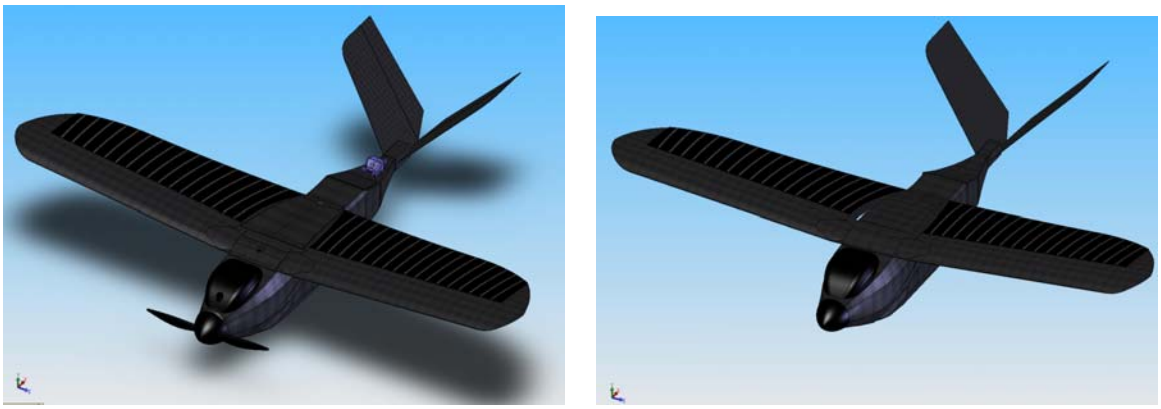

(a) Original model. (b) Simplified model.

Figure 4.2: Simplification of Nighthawk model in SolidWorks®.

ther work in Gridgen®. Since the wind tunnel tests were performed at 0° roll and 0° yaw, the model was considered to be symmetric about the longitudinal plane and the database entities were removed from the right half of the aircraft. This simplification is not entirely accurate since all aircraft experience at least a small amount of asymmetry. Asymmetry is unavoidable in the case of the Nighthawk since it is made of hand-laid carbon fiber. However, the asymmetric effects should be small. Another assumption is that the initial geometry of the Nighthawk (including the wing) is the same for both the stiff wing and the flexible wing. Although the wing shapes are similar, they are not exactly the same because they are hand-made. Figure 4.3 displays the aircraft surfaces that were used to build the aerodynamic grid around the Nighthawk.

The following steps were performed in Gridgen® to build the unstructured surface grids. Database entities were shifted to align properly and gaps were filled with surface patches. Grid surfaces were built on the entire aircraft with a high concentration of grid points near the leading and trailing edges of the wing. Grid surfaces were built to represent the wind tunnel test section—larger spacing was used since the wind tunnel walls were modeled as inviscid. A different grid was built for each AoA with the Nighthawk model rotated to the appropriate angle within the wind tunnel grid. The surface grids were saved in NAsa STRuctural ANalysis (NASTRAN) format. Further details of how the grids were built are included in Appendix E.

4.3 Obtaining the Static Target Displacement

In aeroelastic analysis, two grids are generally considered—a structural grid and an aerodynamic grid. These grids are not required to share the same vertices. The TPS method is commonly used to map the displacements in one grid to the displacements in another [25,32]. In this effort, the TPS method was used to map the displacement of the photogrammetry targets on the wing (i.e. the structural grid) to the displacement of the vertices in the aerodynamic grid.

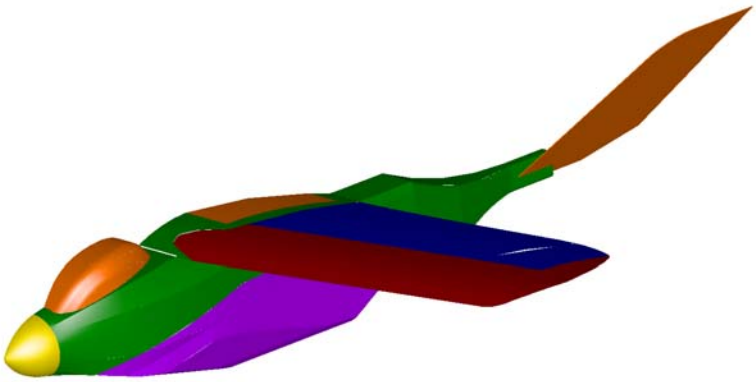

Figure 4.3: Surfaces of Nighthawk used to build aerodynamic surface grids.

The 3-D location of each deflected target was measured as described in Chapter III and exported to a text file. The undeflected (or no-wind) location of each target was recorded in a separate text file. Both files were sorted to ensure the targets in the deflected file were listed in exactly the same order as the targets in the no-wind file. The static displacement of each target was determined by subtracting the average location (over 100 frames) of the deflected target from the no-wind location of the target.

The following algorithm was used to determine the static displacement of the targets on the wing.

1. Read the deflected target locations.
2. Read the no-wind target locations.
3. Sort the targets by location- first in x, then in z. (Perform the sort for the deflected target location and the no-wind target location.)
4. Calculate target deflection by subtracting the no-wind location from the deflected locations.

Sorting the targets in step 3 was critical. If they were not sorted correctly, the calculated displacements would be erroneous. For example, the deflected location of one target may be subtracted from the no-wind location of a different target. The details of the sort algorithm in step 3 are:

1. Clone the matrix of target locations.
2. Append an index number to the cloned matrix.
3. Rotate all target points in the cloned matrix about the origin by an angle of AoA + 6. The rotation is greater than the actual AoA to compensate for the angle of incidence of the wing. *Note: The actual locations of the targets were not altered. The clone matrix was rotated and sorted then the target matrix was reordered according to the sort performed on the clone.*
4. Define cutoff values in x to sort the targets into bins by x-coordinate.
5. Sort the targets in each bin by z-coordinate.
6. Reorder the original matrix of target locations according to the sorted index order.

Figure 4.4 illustrates the need to rotate the target points about the origin before sorting. The dotted lines represent the bin boundaries. Notice from Figure 4.4 (a) that at high AoAs, the target displacements are large enough that there is no way to define a boundary between bin 5 and bin 6 that would keep the no-wind targets in the same bins as the deflected targets. Yet, Figure 4.4 (b) demonstrates that after rotation the targets deflect upwards rather than up and back. After the rotation it is possible to define bin boundaries that are consistent for both deflected and no-wind targets.

Once displacements were obtained for each target, those displacements were used to determine the shape of the wing in the aerodynamic grid. The location of each aerodynamic grid point on the wing was calculated using the TPS method.

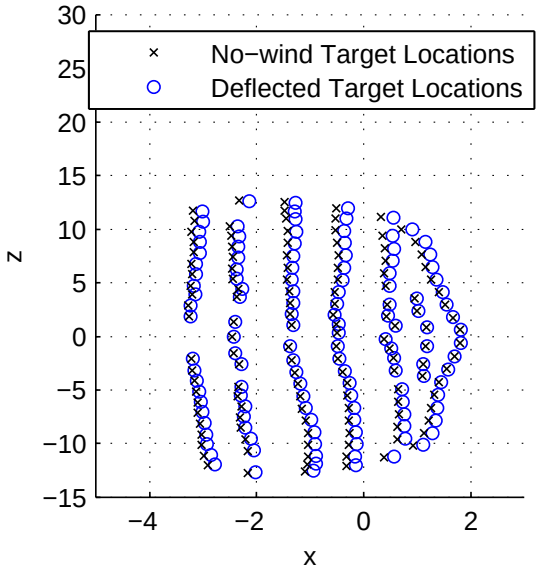

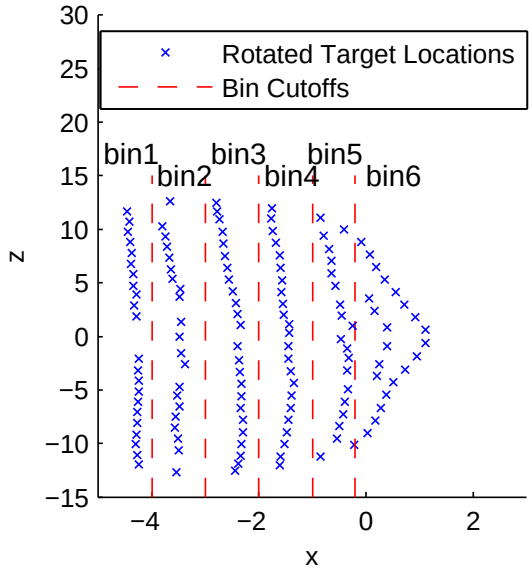

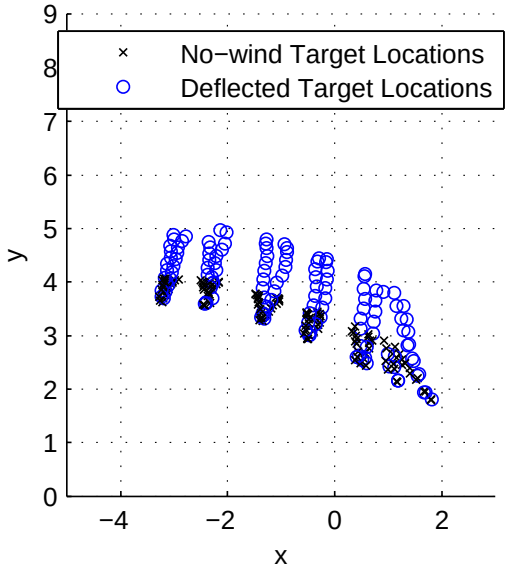

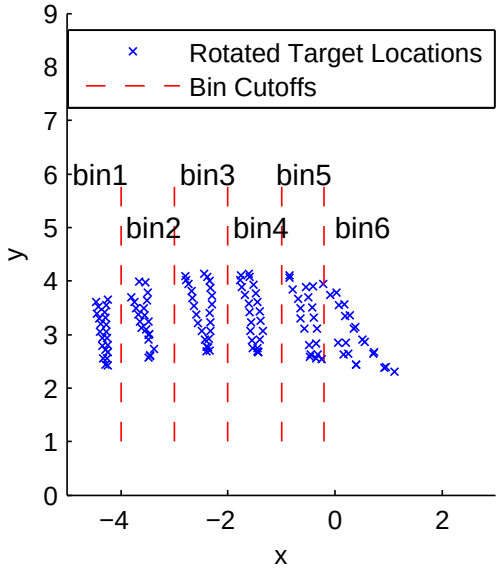

(a) Top and side views of raw target measurements at 14° AoA, 30 mph, flexible wing.

(b) Bin cutoff values for 14° AoA.

Figure 4.4: Illustration of the need to rotate and sort the target displacement measurements.

4.3.1 Adjusting the Aerodynamic Grids Using a Thin Plate Spline. Thin Plate Splines (TPS) are used in aeroelastic applications to relate the motion of a structural grid to the motion of an aerodynamic grid. The structural grid points do not need to be coincident with the aeroelastic grid points. Given the displacement of each target, the displacement of each aerodynamic grid point can be calculated by solving a problem similar to obtaining the minimum energy in a beam [13, 25].

Since the wing structure is non-linear, a different TPS matrix was obtained for each of the 60 different test cases. Parker provides a method for obtaining the TPS matrix [25] based on Duchon's work [13] with thin plate splines. After the TPS matrix was developed, the deflection of each aerodynamic grid point was calculated using equation 4.1. The aerodynamic grid points were then shifted according to the displacement vector calculated below.

$$\delta_a = T\delta_t \tag{4.1}$$

Where δ_a and δ_t represent the static deflection of the aerodynamic grid and the targets respectively, and T represents the TPS transformation matrix.

The aerodynamic grids that were built using the CAD model represent the undeformed wing shape. The TPS method described above was used to calculate the deflection of each grid point on the wing. The NASTRAN files were opened and the locations for the grid points on the upper and lower wing surfaces were overwritten with the deflected locations calculated using the TPS method. The locations of some grid points were fixed to prevent interference between grid surfaces. The gridpoints that were common to the upper wing surface and the symmetry plane were fixed. The grid points common to the lower wing surface and the fuselage were also fixed. The MATLAB® code to implement the TPS method is contained in Appendix D.

Figure 4.5 shows the grids for an AoA of 10° and a speed of 40 mph. The lowest wing is the undeflected wing shape (or rigid wing), the middle wing is the adjusted grid for the stiff wing, and the highest wing is the grid over the flexible wing. The

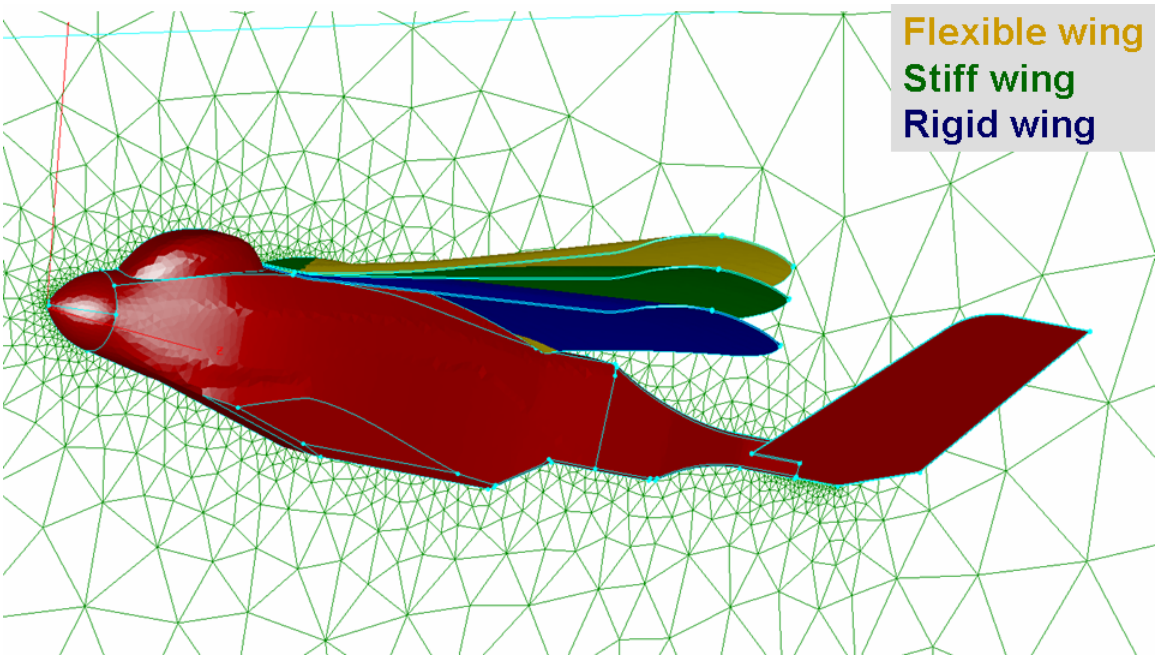

Figure 4.5: Overlapping grids illustrating the difference in wing shapes at 10° AoA and 40 mph.

vertical deflection at the wing tip for the flexible wing is almost 1 inch. Note: the grid displayed here does not represent the actual spacing of the grid points on the symmetry plane.

4.4 Obtaining the 3-D Grids Using SolidMesh

After the NASTRAN file was adjusted to incorporate the deflected wing shape, the file was imported into SolidMesh. SolidMesh is a grid generation package developed by the Computational Simulation and Design Center at Mississippi State University. It uses an Advancing-Front/Local-Reconnection (AFLR) algorithm for grid generation [16]. SolidMesh used the surface grids contained in the NASTRAN file as a starting point for building the 3-D grid.

Both laminar and turbulent grids were built. The only difference between the two was the initial spacing off the wall. For laminar grids the initial grid spacing was calculated to allow ten grid points within the boundary layer. The boundary layer thickness was calculated in SolidMesh using the Blasius flat plate laminar boundary

layer thickness equation [35],

$$\delta_{99} = \frac{5x}{\sqrt{Re_x}} \tag{4.2}$$

Where δ_{99} is the 99% boundary layer thickness, x is the length along the flat plate, and Re_x is the Reynolds Number based on x.

The inputs required to determine the laminar grid spacing were:

- Boundary Layer Fraction (= 0.038523 to allow ten grid points within the boundary layer).
- Reynolds Number (see Tables A.1 and A.2).
- Reference Length (= 6 in based on root chord).
- Max Growth Rate (= 2.0).

The turbulent boundary layer spacing was calculated to allow the first grid point to be located at approximately $y^+ = 1$. The inputs required to determine the turbulent grid spacing were:

- y^+ (= 1 to allow one grid point within the laminar sublayer).
- Reynolds Number (see Tables A.1 and A.2).
- Reference Length (= 6 in based on root chord).
- Max Growth Rate (= 2.0).

The aircraft surfaces were treated as viscous surfaces and the wind tunnel walls were assumed to be inviscid as mentioned in section 4.2. Boundary conditions for viscous surfaces were set to Normal Growth and Reconnect, but boundary conditions for inviscid surfaces, inlets, and outlets were set to Reconnect. The symmetry plane was set to rebuild. The final volume grids consisted of approximately 1.1 million mixed prism, pyramid, and tetrahedral cells. After the 3-D volume grids were generated in SolidMesh, they were exported as FLUENT® case files.

4.5 Obtaining Flow Solutions in FLUENT®

FLUENT® was used as an implicit solver to obtain steady-state solutions to the Navier-Stokes equations. A no-slip boundary condition was applied to all aircraft surfaces, but a slip boundary condition was applied to the wind tunnel walls. The slip boundary condition was applied to model inviscid flow at the wall. This greatly reduced the number of cells required near the wind tunnel walls. An outflow boundary condition was applied to the exit plane and an inlet velocity boundary condition was applied to the inlet plane. The freestream velocity, reference pressure, and reference density for each test case are recorded in Tables A.1 and A.2.

Predicting the location where the boundary layer transitions from laminar to turbulent is a challenging feat. Transition to turbulence is highly sensitive to freestream turbulence, surface roughness, and adverse pressure gradients. The flow solver provides the option to model the entire flow as either laminar or turbulent. Both laminar and turbulent solutions were computed for each AoA and wind speed. However, given the surface roughness and the amount of movement in the wing, the majority of the flow over the wing was expected to be turbulent. For this reason, only the turbulent solutions are presented. A list of actions performed in FLUENT® and sample laminar and turbulent FLUENT® scripts are provided in Appendix F.

Spalart-Allmaras was selected as the turbulence model because it requires less "tuning" than the k-ϵ or k-ω models. This is because Spalart-Allmaras is a one-equation turbulence model with fewer coefficients than the two equation models. Spalart-Allmaras was the natural choice of turbulence models since no experimental data was available to tune the k-ϵ or k-ω models. It should be noted that Spalart-Allmaras is more dissipative than the higher order turbulence models. However, it is also more robust.

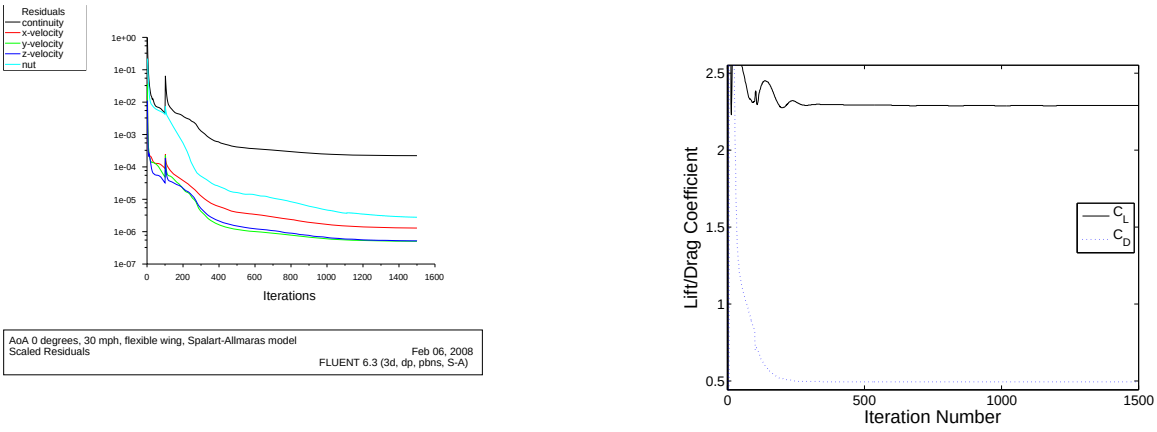

(a) Residuals.

(b) Force histories.

Figure 4.6: Convergence typical for AoAs less than 10°.

4.6 Solution Convergence

The CFD solutions were obtained by solving the incompressible Navier-Stokes equations iteratively. Each iteration contains some error so it becomes a judgment call when the solution has reached steady-state. One way to judge the solution is to monitor the residuals. Residuals are a measure of the error in the solution. To measure the progress towards achieving the solution, the residual on the first iteration is normalized to a value of one. As each iteration is accomplished, the magnitude of the residual is compared with the residual from the first iteration. When the residuals have been reduced to several orders of magnitude less than one, the solution has converged. Another method of determining solution convergence is by monitoring the pressure forces until they reach a constant. This method is usually employed when residuals have leveled off or settled into an oscillatory pattern.

Figure 4.6 is representative of the convergence for AoAs less than 10°. In these cases the residuals settled to just above 1e-4, but the force histories settled out well within 1,500 iterations. The forces monitored in the force history were the lift coefficient and the drag coefficient on the wing surface only.

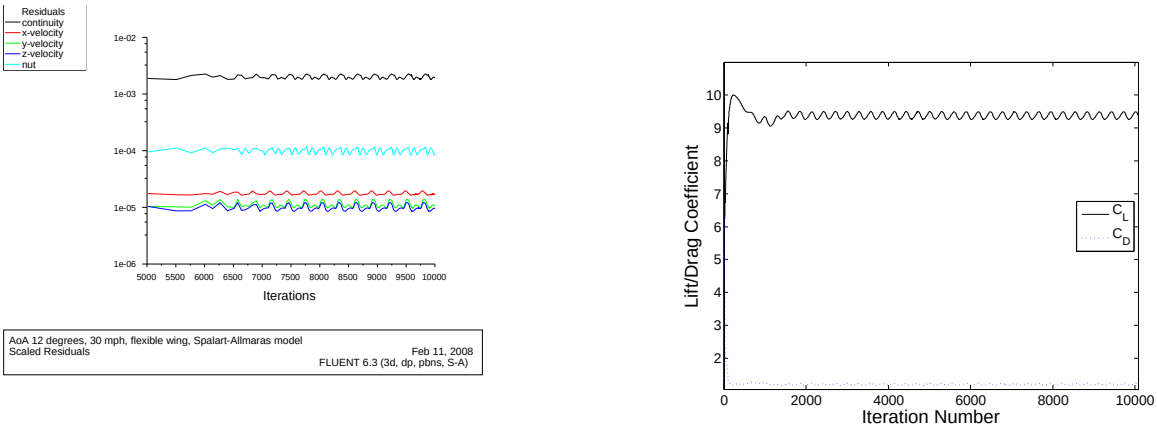

(a) Residuals.

(b) Force histories.

Figure 4.7: Convergence typical for AoAs greater than 10°.

For AoAs greater than 10°, the residuals did not settle to 1e-4. In addition, the force histories developed an oscillatory pattern. The oscillation in the force histories was sinusoidal, which is a classic sign of unsteady shedding. Figure 4.7 shows the typical convergence behavior of residuals and force histories for AoAs greater than 10°. The mean solution was used for each solution that exhibited oscillatory behavior of residuals.

To determine whether the solution was appropriately converged, a time-accurate solution was obtained. The force histories calculated in the time accurate solution were compared with the histories calculated in the steady-state solution. Figure 4.8 shows the comparison between the force histories for the time-accurate solution and the force histories for the steady-state solution for 12° AoA, 40 mph, flexible wing. The oscillations in the time-accurate force histories indicate the presence of unsteady structures in the flow. The mean of the time-accurate force histories matched the mean of the steady-state force histories to within 1.3%. Although the steady-state solution has oscillations, it has reached a point where the solution is acceptable.

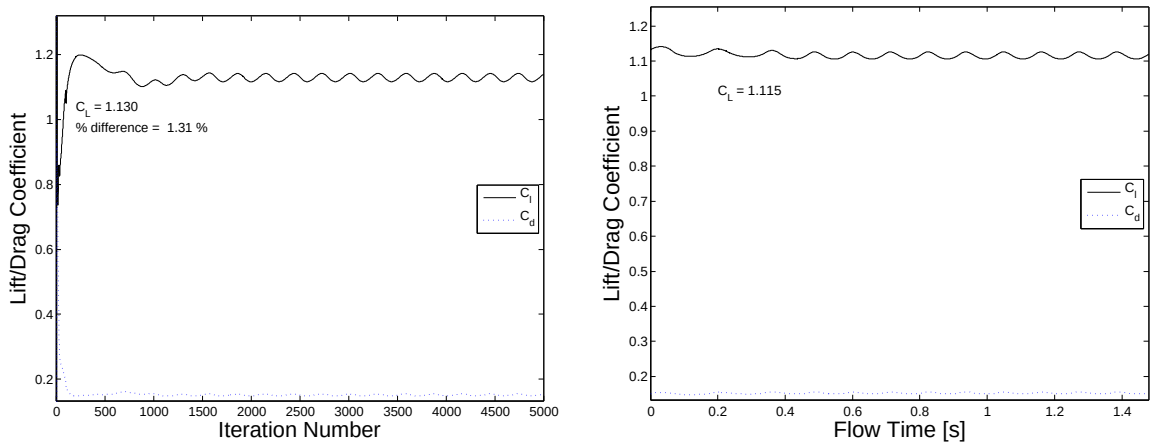

(a) Steady.

(b) Time accurate.

Figure 4.8: Comparison of steady-state force histories with time accurate forces.

4.7 Post Processing

The lift coefficient curve, $C_{L\alpha}$, was determined by integrating the pressure and wall shear stresses over the entire aircraft at various AoAs. Similarly, the moment coefficient curve, $C_{M\alpha}$, was determined by integrating the moment over the entire aircraft. The drag polar was determined by integrating lift and drag over the entire aircraft at various AoAs. These integrations were performed in FLUENT®.

Data was exported from FLUENT® into FieldView to create surface pressure plots for various flight conditions. FieldView was also used to create streamline plots to investigate the interaction between the wing and the tail. The lifting line of the wing was determined by integrating the pressure around the airfoil section at various span-wise locations. The results of this post processing are presented in Chapter V.

V. Results

This chapter contains the results and analysis of the CFD solutions. The aerodynamic performance of each wing is analyzed. Performance comparisons are made between the flexible, stiff, and rigid wings.

5.1 Static Wing Shape

An obvious difference between each wing is the wing shape during flight. As mentioned earlier, the rigid wing is a fictitious wing that has absolutely no deflection relative to the CAD geometry. The stiff wing has some deflection and the flexible wing has the most deflection. The amplitude of deflection of the stiff and flexible wings is dependent upon the flight speed and the AoA. As either the flight speed or the AoA increases, the leading edge of the wing twists downward, increasing the wing tip washout. The entire wing also bends upward, increasing the dihedral of the wing. The deflections of the wings are discussed in detail in the current section. The importance of the results discussed here should not be underestimated. Understanding the deflection in the wing is the key to analyzing the aerodynamic forces obtained through CFD.

All deflections discussed in this section are referring to static or time-averaged deflections. For AoAs below 0° and wind speeds of 30 to 40 mph there was significant motion in the wing (up to 1.5 inches peak-to-peak at the wing tip). There was also some motion (less than 0.25 inches) at AoAs greater than 10° and wind speeds of 40 mph.

To illustrate the wing bending, the static out-of-plane location of the wing was plotted verses span in Figure 5.1. It was plotted for each wind speed at 13.4° AoA. Several cuts were made at different span-wise locations along the wing. The maximum y-location was determined for each cut. These deflections will be used later when the first bending mode will be subtracted from the vertical deflection contours to isolate the effects of higher bending modes. The wing displacement was calculated from the y-displacement and the AoA. The wing displacement was then plotted against span

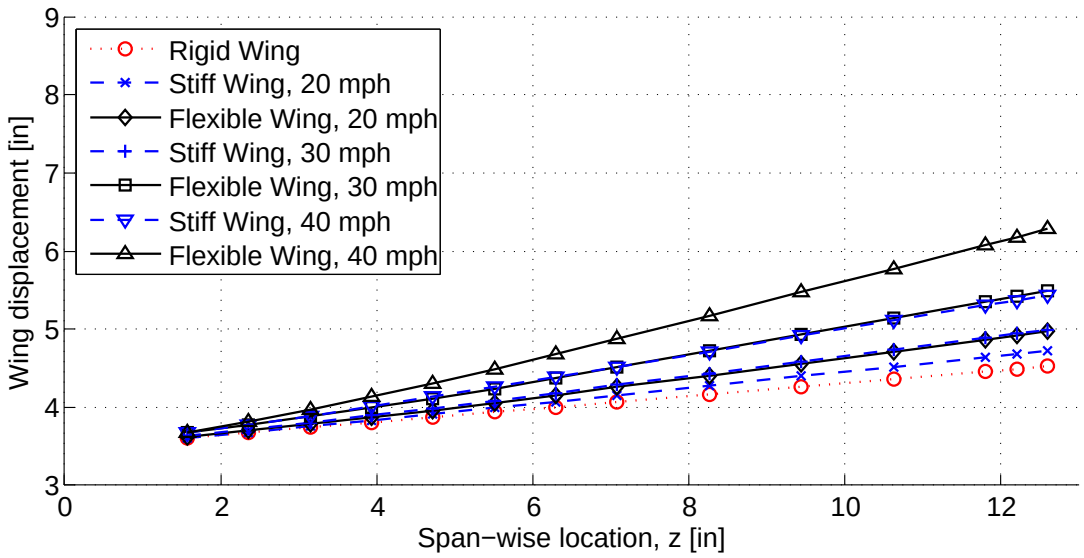

Figure 5.1: Static wing bending at 13.4° AoA, $x \approx \frac{c}{4}$.

to show the upward deflection of the wing. This is an approximation to the bending at $\frac{1}{4}$ chord. While Figure 5.1 is similar to the first bending mode, strictly speaking, the deflections plotted here are not the first bending mode. No structural analysis has been performed so the first bending mode is unknown. However, the deflections in Figure 5.1 will be referred to as the first bending mode throughout the remainder of the document.

Wing tip deflection and dihedral can be obtained from the information in Figure 5.1. The maximum wing tip deflection was 2.6 inches for the flexible wing and 1.8 inches for the stiff wing. At 40 mph the dihedral was 13.2° for the flexible wing, 9.1° for the stiff wing, and 4.6° for the rigid wing. The bending at lower AoAs followed the same trend, but was less pronounced.

Figure 5.2 contains contours of vertical displacement of the wing typical of AoAs less than 2°. This contour pattern is common for this range of AoAs. The deflection was calculated from the difference in the y-coordinate between the rigid wing and the flexible or stiff wing. Deflections are reported in inches. The amplitude of deflection increases with increasing velocity, but the trend is the same. The contours show a significant amount of washout. The flexible wing experiences larger deflections than

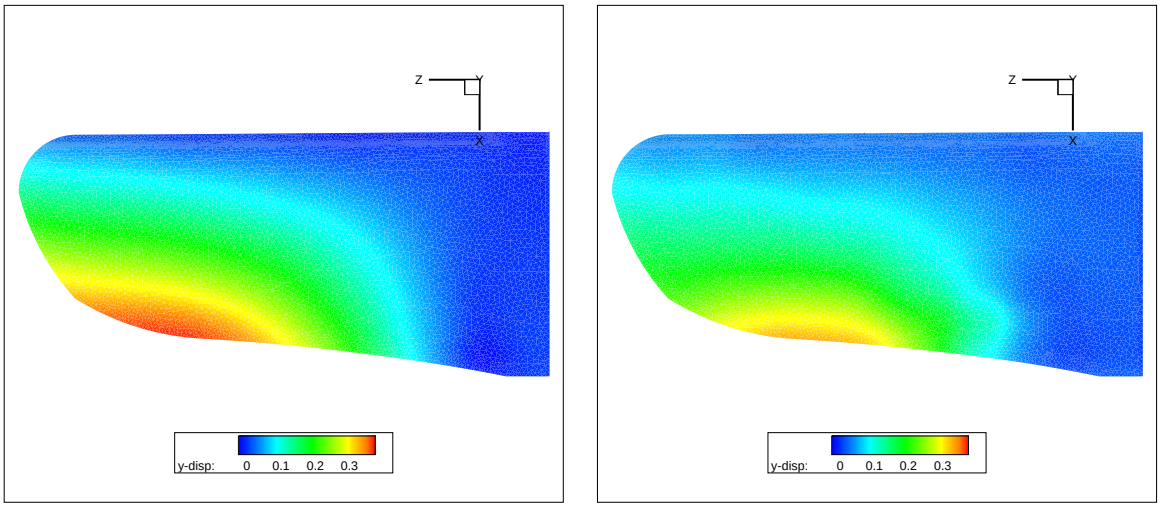

(a) −0.95° AoA, 30 mph, flexible wing.

(b) −0.95° AoA, 30 mph, stiff wing.

Figure 5.2: Measured contours of static wing deflection at low AoAs [in].

the stiff wing. In addition, the flexible wing experiences washout near the wing tip, while the stiff wing experiences washout in a localized region from about 50% span to about 75% span.

Figure 5.3 shows contours of vertical wing deflection at 5.10° AoA. These contours are typical of mid-range AoAs (between 4° and 10°). For mid-range AoAs, the deflection is concentrated more toward the wing tips for both the flexible wing and the stiff wing. However, the washout still occurs further inboard on the stiff wing than the flexible wing. As the AoA is increased, the deflection in the first bending mode increases, making the wing more resistant to deflection in torsion modes (i.e. twist).

Figure 5.4 portrays typical static wing deflection for AoAs greater than 10°. For these high AoAs the deflection is concentrated mostly toward the wing tips for both the flexible and the stiff wings. The pattern and location of washout is similar between the flexible and the stiff wings. The only major difference is in the magnitude of deflection. The flexible wing has about 50% more deflection than the stiff wing at high AoAs.

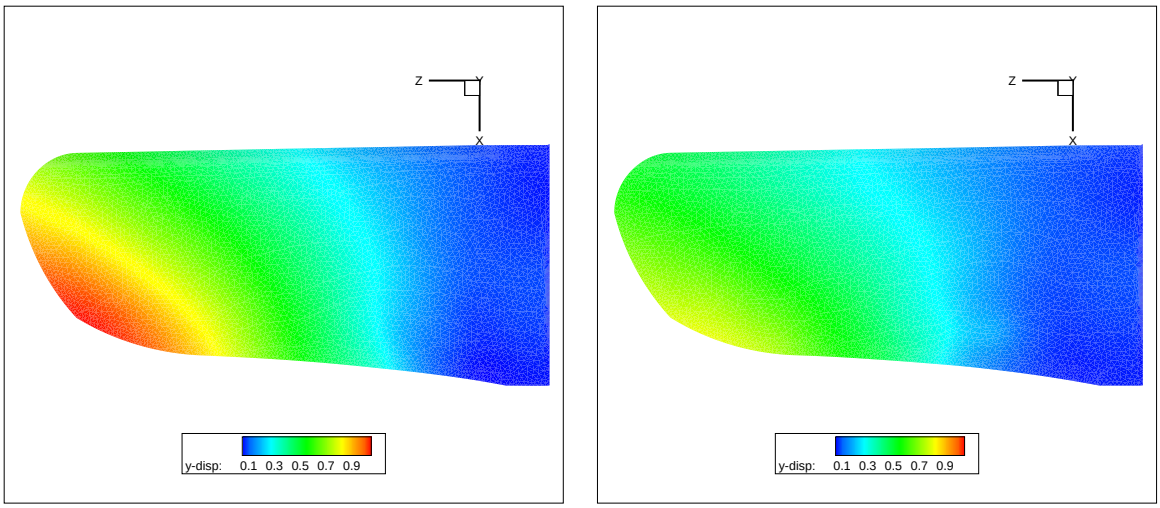

(a) 5.10° AoA, 40 mph, flexible wing. (b) 5.10° AoA, 40 mph, stiff wing.

Figure 5.3: Measured contours of static wing deflection at mid AoAs [in].

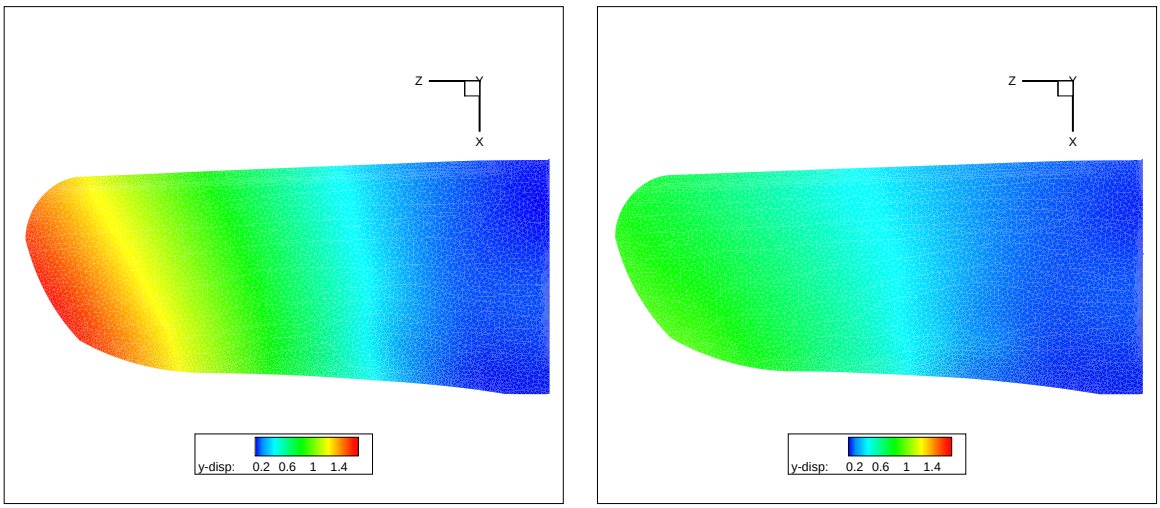

(a) 11.40° AoA, 40 mph, flexible wing. (b) 11.40° AoA, 40 mph, stiff wing.

Figure 5.4: Measured contours of static wing deflection at high AoAs [in].

The discussion surrounding Figure 5.1 focused on the first bending mode of the wings. When the first bending mode is subtracted from wing deflections, the torsional mode is revealed. Figure 5.5 shows displacement contours for the torsional mode at low AoAs and high AoAs. It was created by subtracting the bending in Figure 5.1 from the vertical displacement contours in Figures 5.2–5.4. There are three significant effects in the torsional mode. First, the wing leading edge is twisted down. This twist begins at about 50% span and is most concentrated at the tip of the wing. Second, there is a section of the wing near the root that is twisted up. Finally, notice that there is an apparent increase in camber at the root of the wing. The pattern of the torsional mode is the same for both wings across the entire range of AoA. The amount of torsional deflection increases with wind speed, however it is relatively independent of AoA and wing stiffness.

A fundamental understanding of wing deflection is the key to understanding the aerodynamic effects of a flexible wing. The flexible and stiff wings both experienced two forms of deflection. First, the wings bent upwards increasing the dihedral. Second, the wings' leading edge twisted downwards outboard of the midspan point with a small amount of upward twist near the root. The flexible wing exhibited greater amplitude deflections in the first bending mode than the stiff wing. An increase in AoA or wind speed increased the amplitude of first order bending. The flexible and stiff wings both exhibited comparable amounts of wing twist and the amplitude of twist decreased slightly as AoA was increased. The nature of these deflections will be used to interpret the aerodynamic effects of a flexible wing.

5.2 Wing Sectional Lift Line

A discussion of wing shape naturally leads to a discussion of the wing's sectional lift line. The sectional lift line gives the lift per unit span of the wing at different stations along the span of the wing. It is produced by taking cross-sectional cuts of the wing at various span-wise locations and integrating the pressure around the airfoil. The component of this integrated pressure that is normal to the direction of

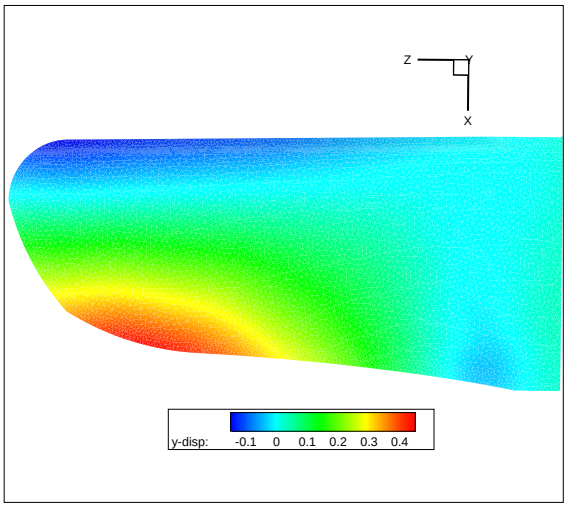

(a) 3.20° AoA, flexible wing.

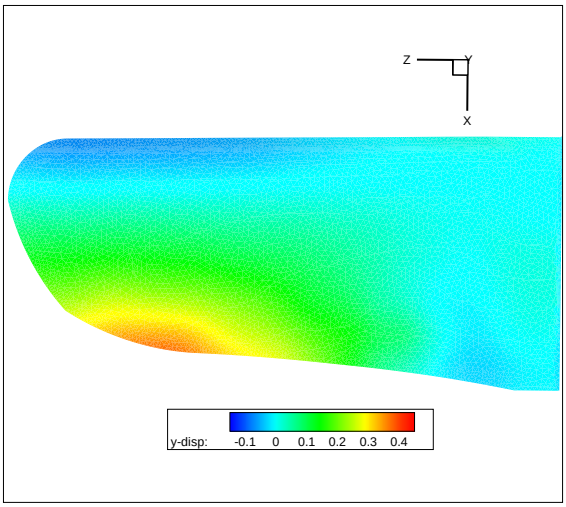

(b) 3.20° AoA, stiff wing.

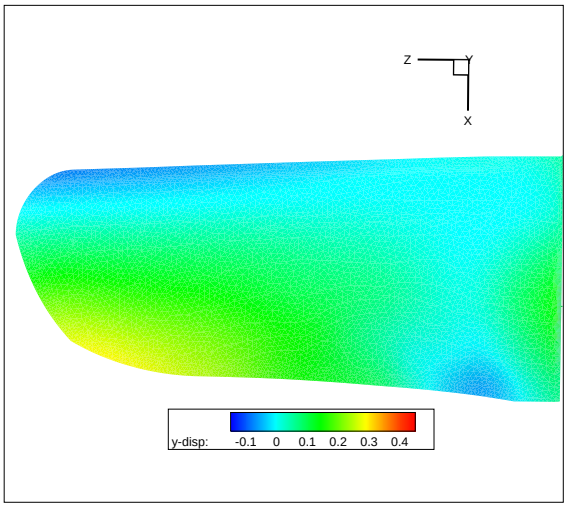

(c) 11.40° AoA, flexible wing.

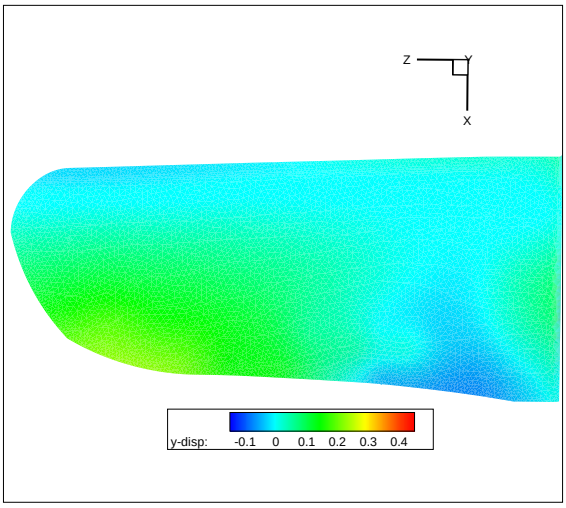

(d) 11.40° AoA, stiff wing.

Figure 5.5: Torsional mode at 40 mph (displacement in inches).

flow is the lift per unit span. The lift line at each cut constitutes a point on the sectional lift line.

The sectional lift line can give clues about flow separation and wing efficiency. The lift line is affected by wing geometry including plan form, sweep, taper, and twist [27]. Prandtl showed that the most efficient wing has an elliptical planform area, assuming it has no sweep and no twist [26]. Such a wing minimizes the induced drag. The lift line for that wing is highest at the root and declines in an elliptic fashion until it reaches zero at the wing tip. Since the Nighthawk's planform is nearly elliptic, the lift line for the rigid wing exhibits a classic elliptic shape for nearly all AoAs and wind speeds. Departure from the classic elliptic shape occurs during wing stall.

The deflections in the flexible and stiff wings result in departure from the classic elliptic lift distribution. This is primarily a result of the twist in the wing. Figure 5.6 gives the lift distributions for all wings and all wind speeds at low, moderate, and high AoAs. Figure 5.6 (a) displays a lift line that is typical of AoAs below 2°. These lift lines are characterized by a massive departure from the classic elliptic lift line on the outboard half of the wing. They also have negative lift at the wingtip. Both phenomena are a result of the twist in the outboard half of the wing shown in Figure 5.2.

For moderate AoAs, the effect of twist is less significant. Figure 5.6 (b) displays the lift line for an AoA of 3.2°. The discussion in Section 5.6 will show that this is the most efficient AoA. The sectional lift line for the stiff and flexible wings are approaching the elliptic shape, but the washout still prevents a pure elliptic shape. It is also clear that the rigid wing provides the most lift, the stiff wing provides slightly less lift, and the flexible wing provides the least lift. This is due to the amount of deflection and twist inherent in each wing.

At high AoAs, the sectional lift line portrays the onset of stall. The drop in the lift line near the wing root in Figure 5.6 (c) indicates that stall occurs at the root

first. Stall advances most rapidly with the rigid wing, next with the stiff wing, and least with the flexible wing. A somewhat surprising but critical observation is that the wingtip does not stall on any wing. It is expected that wingtip washout would prevent tip stall for the flexible and stiff wings, but even the rigid wing does not experience tip stall for the conditions tested. There is a clear opportunity to increase the lift on the wing by increasing twist and producing a higher AoA at the tip. This will be discussed in greater detail in Chapter VI.

5.3 Flow Separation

The onset of stall at high AoAs was discovered using sectional lift lines in Section 5.2. Further flow characteristics can be discovered using surface constrained streamlines (or oilflow images), iso-surfaces, and pressure contour plots. In Section 5.2 the departure from an elliptic lift line was attributed to wing washout. There is another lift-reducing agent acting at low AoAs. This agent is a leading edge vortex on the underside of the wing. Since the wing is thin and highly cambered, at low AoAs the incoming flow has too much momentum to remain attached to the underside of the wing in the vicinity of the leading edge. The flow separates off the leading edge and forms a region of low pressure under the wing near the leading edge. Leading edge vortices are a common design feature that generate lift for many wings. However, in order to generate lift, the flow must separate off the upper surface. Since this vortex forms under the wing it is harmful to overall lift.

The character of the flow typical of low AoAs (less than 8°) is portrayed in Figure 5.7. The surface constrained oilflow shows that flow remains attached on the upper surface of the wing (Figure 5.7 (a)). However, a leading edge vortex accompanied by a separation bubble forms under the wing (Figure 5.7 (b)). The extent of the separation bubble is approximated using an iso-surface of constant x-velocity, u, where $u = -0.001$ m/s. This separation bubble exists at low to moderate AoAs. As AoA is increased, the separation bubble shrinks. The bubble is completely gone at AoAs greater than 10°. However, since typical flight AoAs are below 10°, there is clearly an

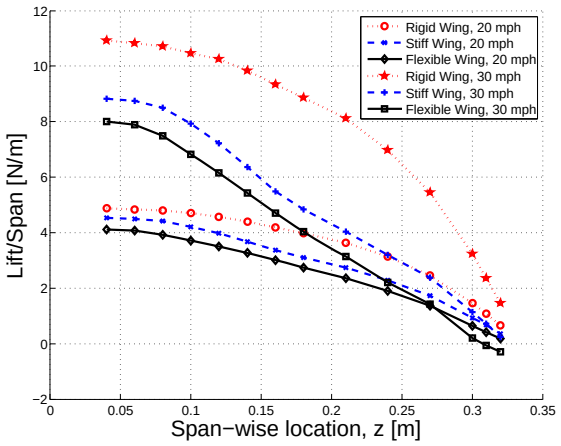

(a) Lift line for $-0.95°$. Typical of low AoAs. Poor performance due to extensive wingtip and midspan washout.

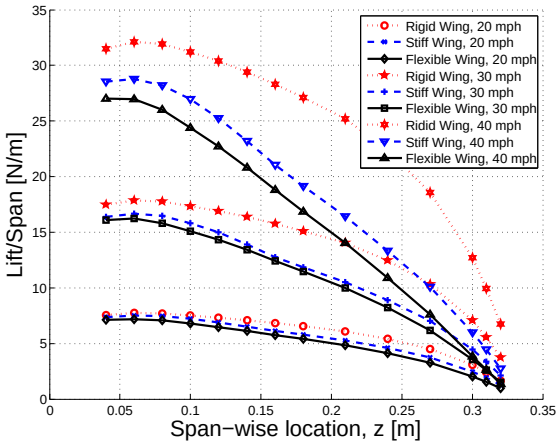

(b) Lift line for $3.20°$ AoA. Most likely design point (from L/D curve). Still enough washout to reduce the effectiveness of the wing.

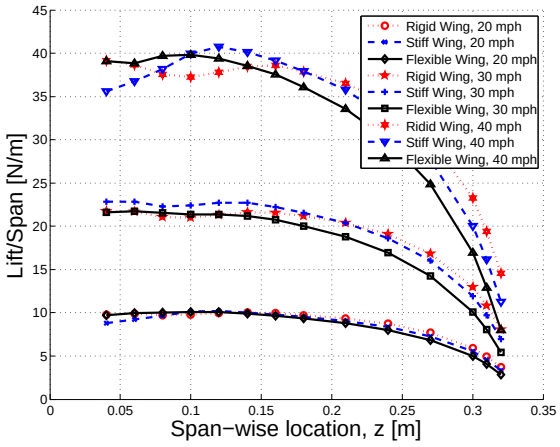

(c) Lift line for $11.40°$ AoA. Stall occurs at the root.

Figure 5.6: Wing sectional lift lines.

opportunity to improve wing performance by reducing or eliminating the separation bubble under the wing.

The separation bubble is viewed in another form in Figure 5.8. Here the extent of the separation bubble is defined by the reattachment point where the surface-constrained flow lines appear to converge. The shading represents surface pressure in Pa, gauge. It reveals the reduction in overall lift caused by the separation bubble when it forms a low pressure region under the wing. The separation bubble is largest for the flexible wing, less extensive for the stiff wing, and smallest for the rigid wing. Wing washout inhibits lift by increasing the extent of the separation bubble. The separation bubble could be reduced or possibly eliminated by either adding thickness to the underside of the wing to keep the flow attached, reducing the camber in the leading edge, or altering the geometric twist in the wing so that the wingtips experience a higher AoA.

As discussed in Section 5.2, the wing experiences stall beginning at the root. More information about the onset of stall can be obtained from oilflow images and iso-surfaces. Figure 5.9 shows the progression of stall as AoA is increased. At AoAs greater than 10° the flow remains attached on the underside of the wing. However, flow begins to separate on the upper surface of the wing at AoAs as low as 6°. There are four possible contributors to separation on the upper surface. These contributors include:

- The angle of incidence at the root, which is 4.82°.
- The flow disturbance from the GPS unit located atop the fuselage between the nose and the wing.
- The increased camber near the root.
- The increased apparent angle of attack due to higher order bending near the root.

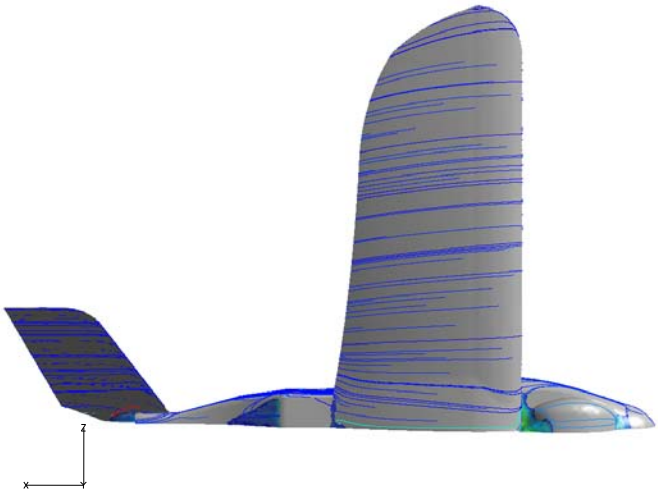

(a) Top view.

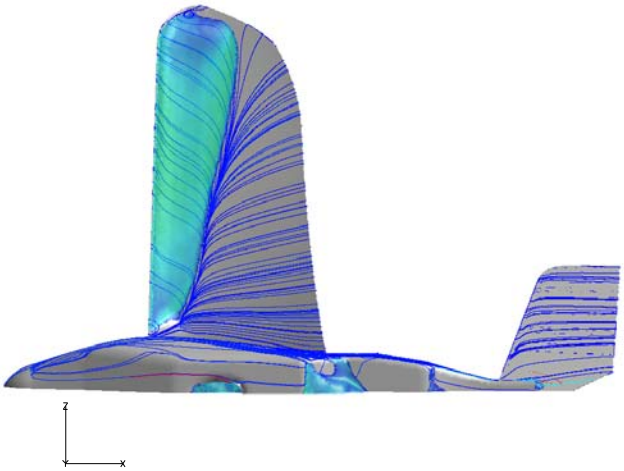

(b) Bottom view.

Figure 5.7: Flow separation under the flexible wing at 3.20° AoA and 40 mph.

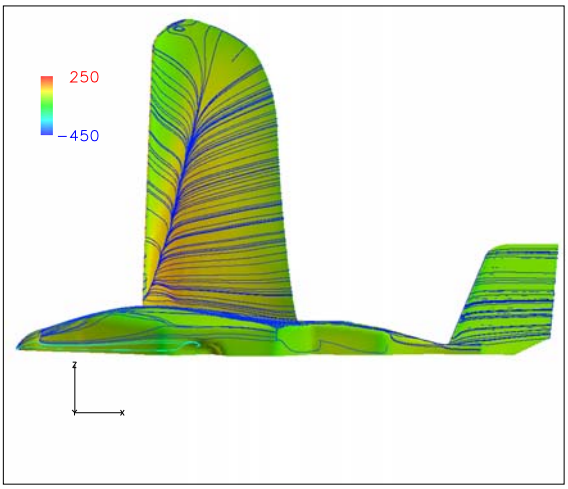

(a) Flexible wing.

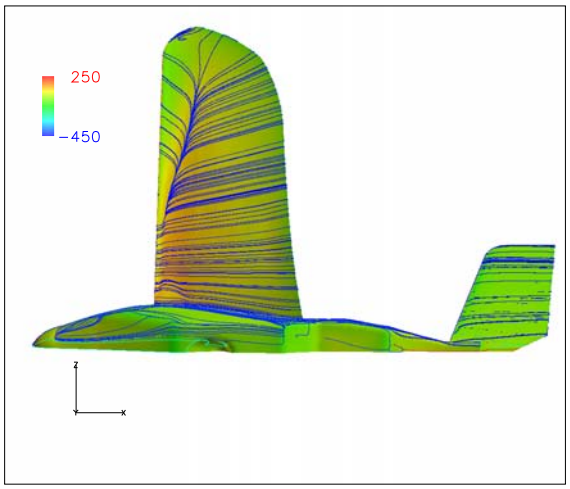

(b) Stiff wing.

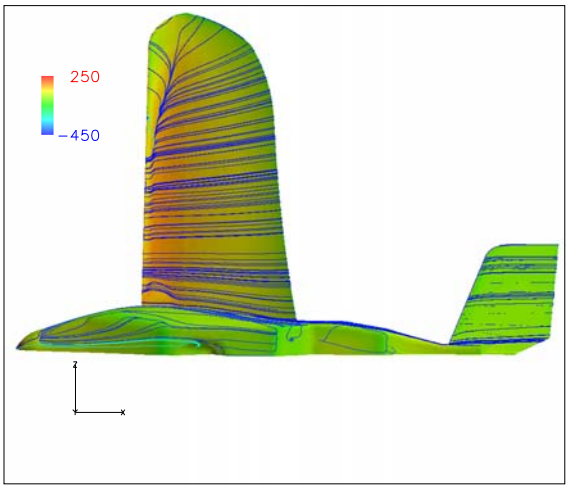

(c) Rigid wing.

Figure 5.8: Flow separation under each wing at 5.10° AoA and 40 mph.

Given that the wing deflection near the root is small, the last two items are not significant contributors to separation. The most significant contributors are the incidence angle and the flow disturbance caused by the GPS unit.

5.4 The Effect of a Flexible Wing on Force Coefficients

Force coefficients can be used to quantify the performance of an aircraft. They are also parameters needed for control algorithms. The force coefficients presented here were obtained by integrating forces and moments over the entire aircraft with no tail deflection. As a result, the magnitude of the moment coefficient may not be representative of the stick-free moment acting on the aircraft, but the trend is comparable.

5.4.1 Lift Curve. The lift curve is a measure of the increase in lift due to an increase in angle of attack. The theoretical lift curve slope can be obtained from equations 2.3 and 2.4. Corrected for AR (9.55) and assuming an Oswald efficiency factor of one, the theoretical lift curve slope is 0.109 $\frac{1}{\text{deg}}$. This represents the highest lift curve achievable from thin airfoil theory.

The lift for each wing was obtained by integrating the pressure and wall shear stress over the entire aircraft and dotting the result with the vertical direction normal to the flow. The lift was then plotted against AoA to obtain the lift curve. Figure 5.10 contains the lift curves for each wing at 20, 30, and 40 mph. In each case, the rigid wing performs the best in terms of having the greatest lift. Similarly, the stiff wing has more lift than the flexible wing for each AoA. The wing deflection of the stiff and flexible wings accounts for the reduced lift compared with the rigid wing.

The lift curve is also used to determine the stall angle. The stall angle is the AoA for which an increase in AoA no longer results in an increase in lift. The stall angle is increased for a flexible wing because washout reduces the effective AoA and provides greater stall resistance. This is seen in Figure 5.10 where the stall angles are approximately 11°, 10°, and 9° for the flexible, stiff, and rigid wings respectively.

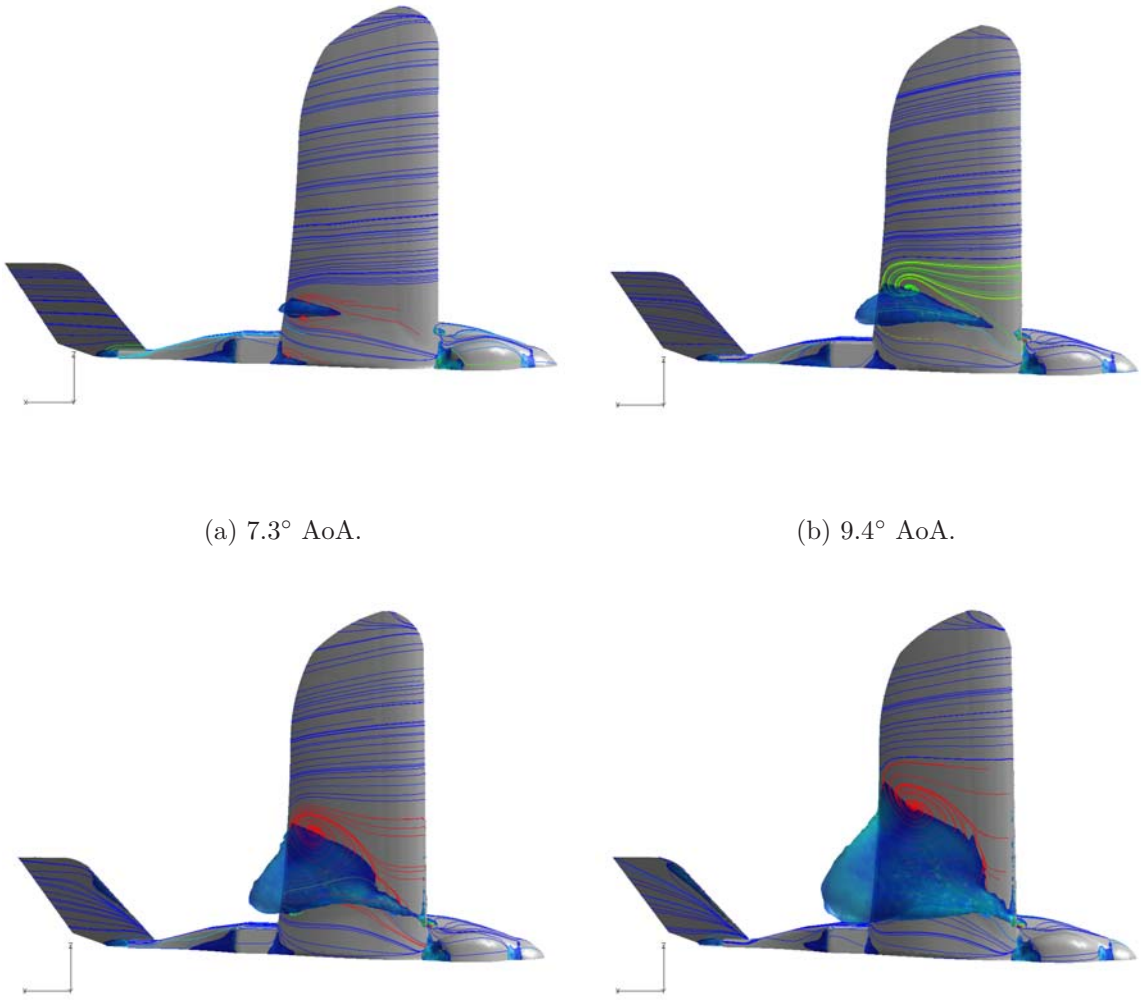

(a) 7.3° AoA.

(b) 9.4° AoA.

(c) 11.4° AoA.

(d) 13.4° AoA.

Figure 5.9: Stall progression on the upper surface of the flexible wing at 40 mph.

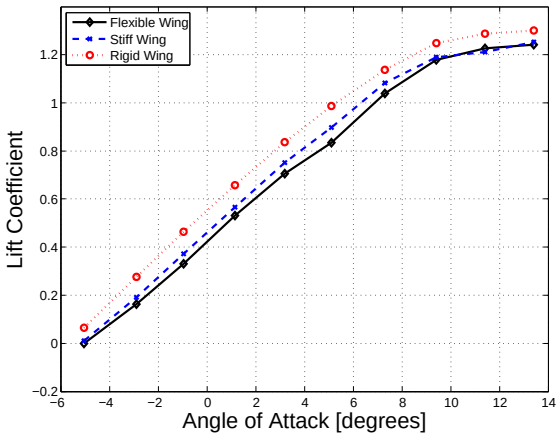

(a) 20 mph.

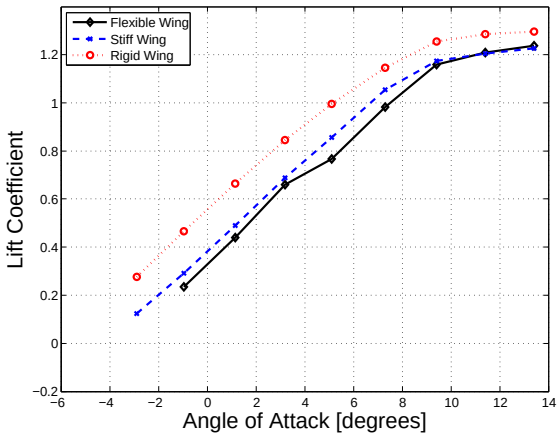

(b) 30 mph.

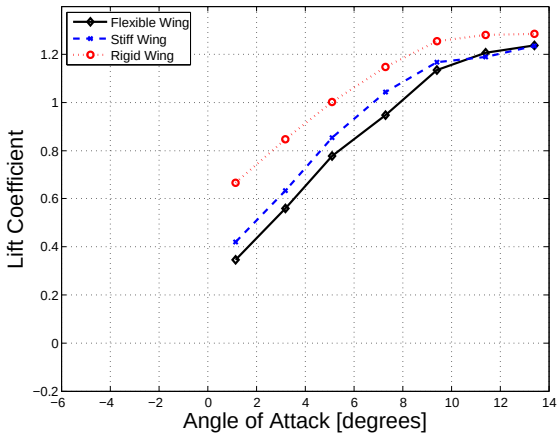

(c) 40 mph.

Figure 5.10: Computed lift coefficients.

The slope of the lift curve is a measure of the efficiency of the wing. To find the lift curve slope, a line was fit through the lift curve of each wing for AoAs less than 8°. The lift curve slope at 20 mph was averaged with the slope of the lift curve at 30 mph for each wing. The slope of the lift curve at 40 mph was ignored because there were not enough data points at low AoAs to get an accurate measurement of the slope. The average slope of the lift curve was 0.0870 $\frac{1}{\text{deg}}$ for the flexible wing, 0.0898 $\frac{1}{\text{deg}}$ for the stiff wing, and 0.0867 $\frac{1}{\text{deg}}$ for the rigid wing. These slopes correspond to Oswald efficiency factors of 80%, 95%, and 79%, respectively. These efficiencies are slightly lower than expected for an elliptical wing because the lift curve was generated by integrating pressure over the entire aircraft rather than integrating pressure over the wing only and because the wing is not truly elliptical.

The lift curve for the flexible wing dips at about 5°–7° AoA. It looks similar to the lift curve when a long laminar separation bubble is present. However, since no laminar separation bubble is present, that is not the cause. Further investigation is required to determine the cause of the dip in the lift curve.

The rigid wing has a lower efficiency factor than the stiff wing because it experiences the onset of stall earlier. This reduces the slope of the curve fit for the rigid wing.

Notice that the zero-lift AoA for the rigid wing is less than the zero-lift AoA for the flexible and stiff wings (See Figure 5.10 (a)). This difference is caused by the difference in the static shape of the flexible and stiff wings verses the rigid wing, which has no deflection. The static deflection of the flexible and stiff wings is similar to the deflection portrayed in Figure 5.2.

5.4.2 Drag Curve. The drag curve was obtained by integrating the pressure and shear stress over the entire aircraft and dotting the result with the flow direction. The drag curve is generally used to determine the power required to cruise at a given AoA. It is also useful in finding the minimum drag. Figure 5.11 shows that the minimum drag is about 0.07 for each wing. The rigid wing has the highest drag across

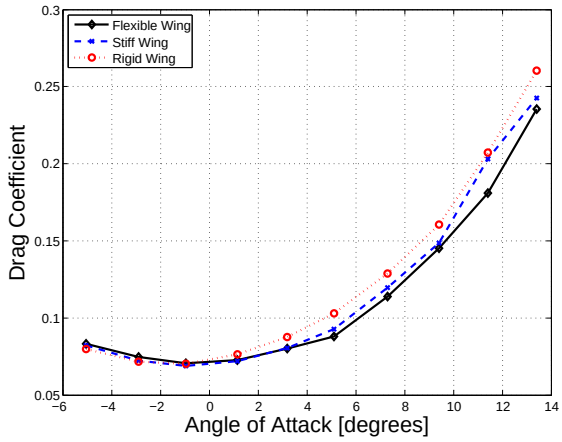

(a) 20 mph.

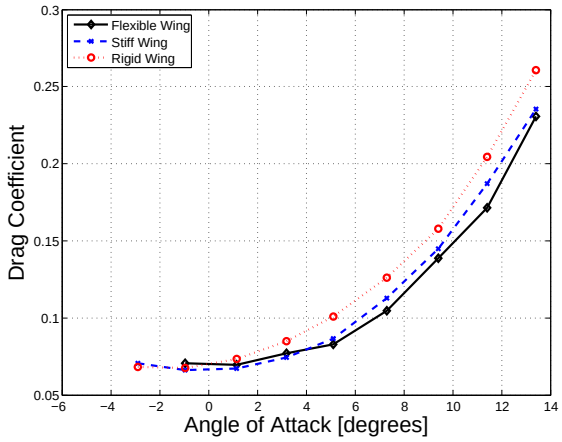

(b) 30 mph.

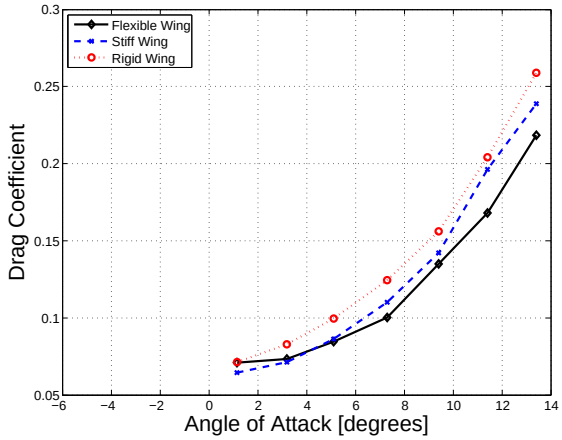

(c) 40 mph.

Figure 5.11: Computed drag coefficients.

the range of AoAs, followed by the stiff wing and the flexible wing, respectively. The drag for the stiff and flexible wings is reduced by washout.

5.5 The Drag Polar

The drag polar was produced by plotting the lift at each AoA and wind speed with the drag at the respective AoA and wind speed. It is generally parabolic. Cambered wings have drag polars that are shifted up on the lift axis. The drag polar can be used to determine the $C_{L\ max}$, which can be used to determine the maximum

payload. Figure 5.12 gives the drag polar for each wing at 20, 30, and 40 mph. For all flight speeds the rigid wing has the greatest $C_{L\ max}$ (approximately 1.29). The stiff wing and the flexible wing have essentially the same $C_{L\ max}$ (approximately 1.21). The rigid wing out performs the stiff and flexible wing in maximum payload.

5.6 Lift-to-Drag Ratio

Lift-to-drag ratio is a measure of the efficiency of an aircraft. This is a critical performance measure since it is closely tied to loiter time and range. As described in Section 2.5.3, the best loiter cruise for a propeller aircraft is $0.866\frac{L}{D}_{max}$ [27]. Figure 5.13 gives $\frac{L}{D}$ of the Nighthawk for each wing and wind speed. Assuming the Nighthawk is optimized for best loiter, the operating AoA for the flexible wing is between 2° and 3°. The operating AoA for the stiff wing is between 1° and 2° and the operating AoA for the rigid wing is 0°.

Figure 5.13 indicates that a flexible wing results in a curve with a lower $\frac{L}{D}_{max}$ than a stiff wing. Washout reduces the lift of the wing and the induced drag of the wing. However, the parasite drag remains almost constant. The net effect is a reduced $\frac{L}{D}$ for a flexible wing. This conclusion differs from DeLuca's findings [10]. He studied a set of reflex wings and found that the flexible wing performed better than the stiff wing both in terms of maximum lift and efficiency ($\frac{L}{D}_{max}$). Perhaps in his case the billowing of the reflex wing improved lift enough to outweigh the loss in lift due to washout.

In addition to reducing the peak in the lift-to-drag curve, a flexible wing also shifts the curve to the right. This shift is a result of decreased lift in a flexible wing at low AoAs and increased stall resilience at high AoAs.

Finally, the band for appropriate flight AoAs is narrowed as speed increases. The left slope of the curves in Figure 5.13 represents a reduced $\frac{L}{D}$ because lift decreases rapidly at low AoAs. The right portion of each curve represents a reduction in $\frac{L}{D}$

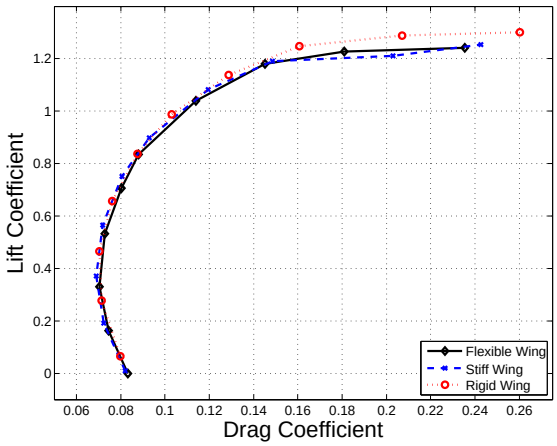

(a) 20 mph.

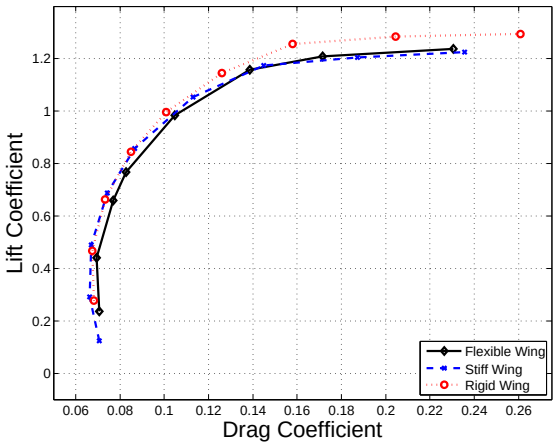

(b) 30 mph.

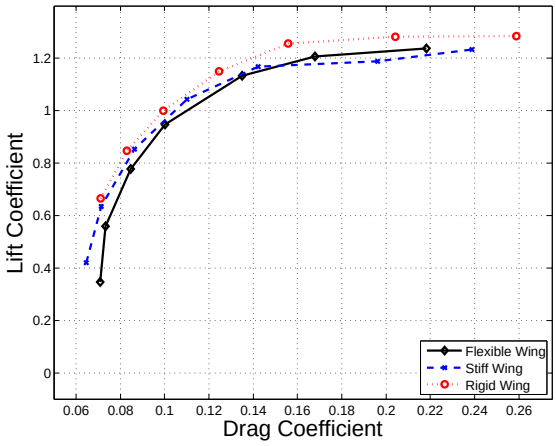

(c) 40 mph.

Figure 5.12: Drag polar.

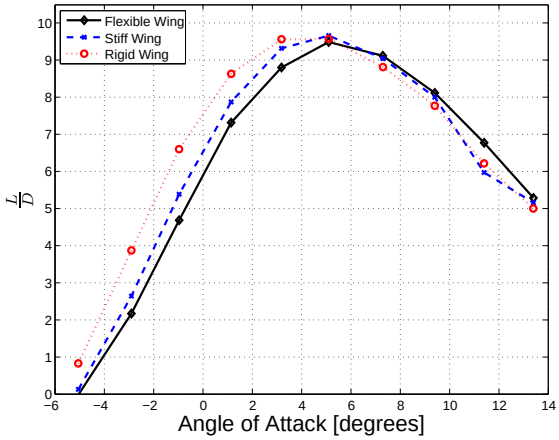

(a) 20 mph.

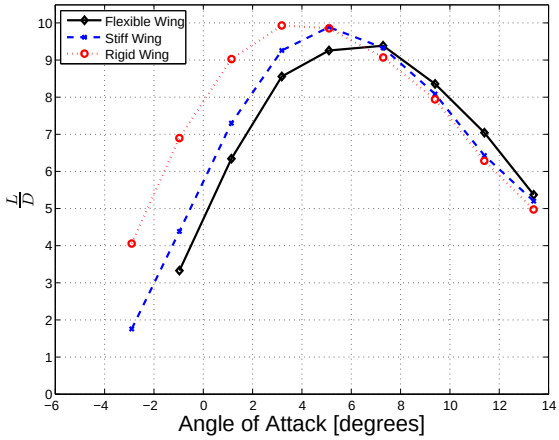

(b) 30 mph.

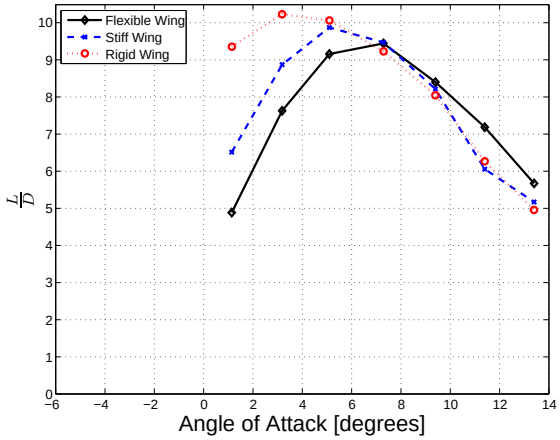

(c) 40 mph.

Figure 5.13: Lift-drag ratio.

due to an increase in drag at high AoAs. As wind speed increases, the slope of these curves increases and the band of suitable operating AoAs shrinks.

5.7 Aircraft Stability

The slope of the pitching moment curve, $C_{M\alpha}$, is used to determine whether an aircraft is stable in the longitudinal axis. The typical reference frame in controls is with the x-axis out the nose of the aircraft, the y-axis out the starboard wing, and the z-axis pointing down. For the purpose of calculating $C_{M\alpha}$, the default coordinate system was transformed to the body-axis system. Using this reference frame, the slope of $C_{M\alpha}$ represents the change in moment about the y-axis with the change in AoA. A negative slope represents a stable system. To illustrate, imagine the aircraft encounters a disturbance that increases the AoA. If $C_{M\alpha}$ is negative, the resulting moment tends to rotate the nose back down. This restoring moment is stable about the trim point (the point on the curve where $C_M = 0$).

Figure 5.14 shows the pitching moment coefficient curve for all wings at each wind speed. It was created by integrating the moment about the center of gravity for each AoA and wind speed. It indicates that all wings are stable for all tested wind speeds. The value of $C_{M\alpha}$ does not vary much from wing to wing. However, the flexible wing has a steeper slope than the rigid wing making it slightly more stable. The slope of the moment curve is highly dependent upon wind speed. Higher wind speeds result in much stronger restoring moments, although they do not change the trim condition.

In the CFD analysis, the ruddervators were fixed with zero deflection. This resulted in a trim AoA of about -1° relative to the body axis. To raise the trimmed AoA, the ruddervators should be deflected upwards, causing a net down force on the tail and raising the AoA. This action translates the moment curve up. Ideally, the trim condition with no ruddervator deflection should be near the operating AoA. This means very little control authority would be required to keep the aircraft flying level.

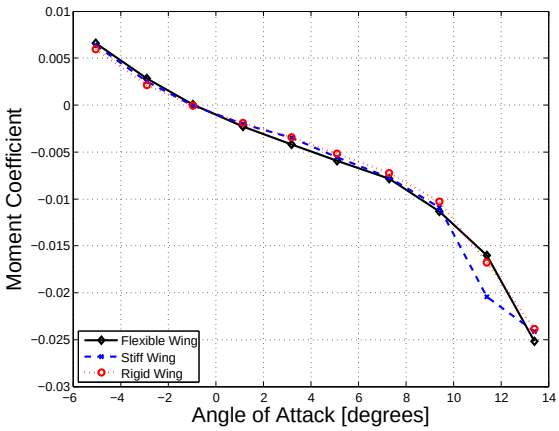

(a) 20 mph.

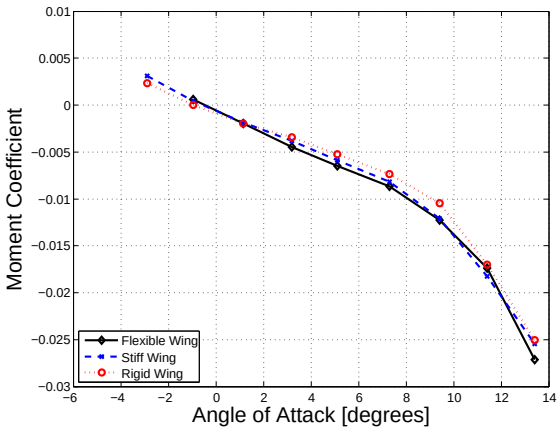

(b) 30 mph.

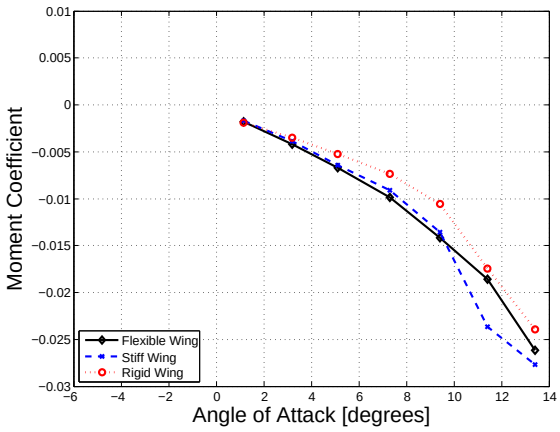

(c) 40 mph.

Figure 5.14: Pitching moment coefficient computed about the center of gravity.

To bring the trim AoA closer to the operating AoA, the angle of incidence of the tail could be reduced slightly.

This recommendation is accompanied with a caveat. The deflection of the tail was not measured during wind tunnel tests. The tail may have significant deflection during flight, causing the actual trim AoA to be different than $-1°$. In addition, the desired ruddervator deflection may not be $0°$ since the tail stiffens dramatically with a small amount of ruddervator deflection. A stiffer tail could improve the flight dynamics making the constant ruddervator input worthwhile. In light of the information presented on pitching moment curve and dihedral, a flexible wing increases the static stability of an aircraft in pitch and roll.

5.8 The Effect of a Flexible Wing on the Tail

An advantage of obtaining CFD solutions is that once the solutions are obtained, all flow parameters are known and visualization options are plentiful. For example, once a solution is obtained, the flow can be analyzed using pressure contours, velocity vectors, streamlines, surface constrained oilflow, and iso-surfaces. Each of these solutions would require its own experimental setup. In addition to analyzing the performance of a flexible wing, a knowledge of the effect of the wing on the tail of the Nighthawk is desired. This analysis will be presented in a qualitative manner.

Figure 5.15 (a) shows streamlines that pass just above the tail surface at the operating AoA. They show that although the tail is in the downwash of the wing, there are no significant performance penalties for the given configuration. The effects of the tail being in the downwash of the wing can be countered by altering the incidence angle of the tail if required. However, as the AoA is increased, the tail moves directly in the wake of the wing. At an AoA of $10°$ there is a separation bubble on the top of the wing and the tail is located directly downstream of the bubble. This certainly will have an effect on the performance of the tail. As higher AoAs are reached, the tail moves low enough that it begins to receive more flow from underneath the wing

than flow that has passed over the wing and has been disturbed by the separation bubble on the upper wing surface.

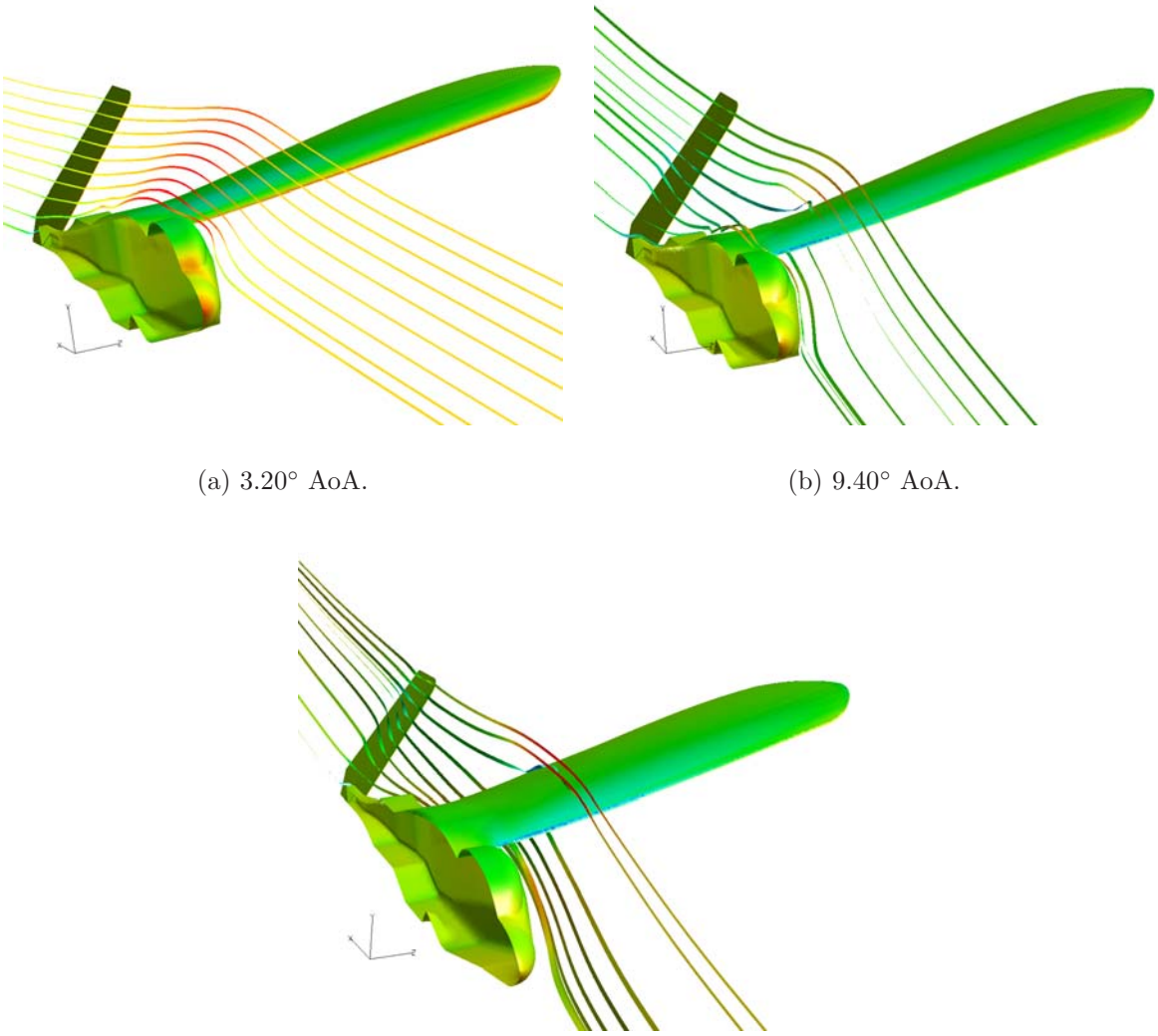

(a) 3.20° AoA.

(b) 9.40° AoA.

(c) 11.40° AoA.

Figure 5.15: Streamlines just above the tail for various AoAs and 40 mph.

VI. Conclusions and Recommendations

The focus of this study was to identify the advantages and disadvantages of using a flexible wing on the Nighthawk mini-UAV. Steady-state CFD solutions were obtained for wind speeds of 20, 30, and 40 mph and AoAs ranging from $-4°$ through $14°$ in increments of $2°$. These solutions were used to analyze the performance of the Nighthawk with a flexible wing, a stiff wing, and a rigid wing.

6.1 Advantages and Disadvantages of a Flexible Wing

There are two primary deformations experienced by a flexible wing in flight. The wing bends upward and the leading edge twists downward on the outboard half of the wing (see Figures 5.1–5.4). These deformations affect the performance and stability of the wing.

The flexible, stiff, and rigid wings were compared in terms of stability and aerodynamic performance. A flexible wing has greater stability than a rigid wing, but its steady aerodynamic performance is degraded.

6.1.1 Static Stability. Static pitch stability was investigated using $C_{M\alpha}$ as a measure of performance and a qualitative analysis of static roll stability was given based on dihedral. $C_{M\alpha}$, and therefore, pitch stability is almost independent of wing stiffness. However, the flexible wing is slightly more stable in pitch than the stiffer wings. The dihedral of the flexible wing was greater than the dihedral of the stiff and rigid wings. As a result, the flexible wing has greater roll stability than the stiff or rigid wing.

6.1.2 Aerodynamic Performance. Aerodynamic performance was analyzed in terms of maximum lift, efficiency ($\frac{L}{D}_{max}$), and stall resistance. The rigid wing had the best aerodynamic performance. It had the highest $C_{L\ max}$ (approximately 1.3 over the entire aircraft) and the highest $\frac{L}{D}_{m}ax$ (approximately 10 depending on flight speed). The flexible wing had slightly greater overall stall resistance due to the washout at the wingtips. However, wing stall originated at the root.

At AoAs less than 8° a separation bubble was discovered under the wing. A leading edge vortex forms due to high camber and a very thin wing. This vortex creates a region of low pressure on the lower surface of the wing, reducing overall lift. It is more prominent in a flexible wing than a stiff wing.

To achieve maximum steady aerodynamic performance the following steps are recommended:

- Use a more rigid wing.
- Reduce or eliminate the separation under the wing at low to moderate AoAs. This can be done by increasing the thickness of the wing or by twisting the wing up. Twisting the leading edge of the wing up is the preferred method because it would increase the lift in two ways: it would increase the AoA for the outer portion of the wing and it would reduce the separation bubble under the wing. Since the wing tip does not stall even at 14° AoA, increasing the twist should not result in a lower stall angle.
- Delay separation at the root by reducing the profile of the GPS unit or by reducing the incidence angle at the root.

Static analysis shows that a rigid wing has greater steady aerodynamic performance. A rigid wing also provides adequate static stability, although it is less than the static stability of a more flexible wing. For these reasons a rigid wing is recommended. However, dynamic stability should be considered before adopting a rigid wing. The Nighthawk mini-UAV carries cameras onboard. For these cameras to be useful, favorable dynamic stability is important. The disturbance initiated by a wind gust should damp out quite quickly to maintain video quality. A flexible wing may have better dynamic stability than a rigid wing due to adaptive washout.

6.2 Future Work

Several hundred gigabytes of image sequences were captured during wind tunnel testing. This data could be used to perform a coupled aeroelastic analysis of the

Nighthawk mini-UAV. The time-accurate measured wing deflections could be used to dynamically update the grid in a time-accurate CFD solution. The dynamic behavior of the flexible wing could be compared with the dynamic behavior of the stiff wing.

During wind tunnel testing, the deflections of the tail were noticeable, but they were not measured. The grid was not updated to reflect the deflections in the tail. Future work could include measuring and including tail deflections and control surface deflections in the CFD analysis.

Forces were not measured during wind tunnel testing. Further wind tunnel testing should be performed to measure the forces during flight. This could be used to validate the current CFD solutions.

The current study is limited to the longitudinal axis. Further measurements and computational analysis could be performed to determine forces, moments, and static stability coefficients in roll and yaw.

CFD loads and measured displacements could be used in attempt to create an effective stiffness matrix. The stiffness matrix could be used to compute flow solutions at other static conditions. For example, a flow solution could be obtained for a different AoA or wind speed.

Appendix A. Test Matrix

This appendix gives the actual AoA and wind speed for each test case. The AoA was confirmed with an inclinometer. For AoAs less than or equal to 0° and high windspeeds (30 to 40 mph) there was too much oscillation to determine a static wing shape. These cases were not tested and are indicated by a dash in Tables A.1 and A.2.

Table A.1: Test Matrix—Flexible Wing.

AoA [deeg]	Speed [mph]	Pressure [in Hg]	Temp [F]	rho [$\frac{kg}{m^3}$]	Re	Solved
-5.05	21.1	28.81	71.9	1.1511	91317	y
-5.05	31.7	28.81	73	1.1490	136942	-
-5.05	42.1	28.83	73.3	1.1489	181857	-
-2.9	21.1	28.88	72.9	1.1518	91375	y
-2.9	31.8	28.88	73.6	1.1503	137529	-
-2.9	42.4	28.89	74.1	1.1497	183280	-
-0.95	21.4	28.89	73.3	1.1516	92656	y
-0.95	31.9	28.9	73.8	1.1506	138003	y
-0.95	42.4	28.9	73.9	1.1505	183410	-
1.15	21.1	28.91	73.5	1.1517	91365	y
1.15	31.8	28.91	73.9	1.1510	137615	y
1.15	42.6	28.91	74.1	1.1506	184297	y
3.2	21.1	28.93	74.3	1.1508	91293	y
3.2	31.9	28.92	73.8	1.1516	138121	y
3.2	42.7	28.92	74.2	1.1508	184763	y
5.1	21.7	29.32	69.4	1.1771	96037	y
5.1	32.3	29.32	69.4	1.1771	142949	y
5.1	43.1	29.31	68.8	1.1782	190924	y
7.3	21.1	28.86	79.5	1.1369	90192	y
7.3	31.8	28.86	79.5	1.1369	135929	y
7.3	42.1	28.86	79.5	1.1369	179957	y
9.4	21.5	28.84	80.7	1.1336	91634	y
9.4	32.2	28.83	81.2	1.1324	137097	y
9.4	42.1	28.83	82	1.1306	178971	y
11.4	21.4	28.79	81.4	1.1304	90951	y
11.4	31.6	28.79	81.4	1.1304	134302	y
11.4	42.3	28.79	81.4	1.1304	179777	y
13.4	21.4	28.79	81.8	1.1295	90881	y
13.4	31.5	28.79	81.8	1.1295	133773	y
13.4	42.1	28.79	81.8	1.1295	178789	y

Table A.2: Test Matrix—Stiff Wing.

AoA [deg]	Speed [mph]	Pressure [in Hg]	Temp [F]	rho [$\frac{kg}{m^3}$]	Re	Solved
-5.05	21.2	28.94	73.3	1.1534	91934	y
-5.05	31.9	28.94	74.6	1.1506	137999	-
-5.05	42.65	28.94	74.7	1.1503	184455	-
-2.9	20.9	28.96	73.6	1.1537	90656	y
-2.9	31.7	28.96	74.5	1.1515	137240	y
-2.9	42.5	28.95	74.5	1.1510	183930	-
-0.95	21.6	28.99	73.2	1.1555	93840	y
-0.95	31.7	28.98	74.4	1.1528	137398	y
-0.95	42.7	28.98	74.4	1.1526	185039	-
1.15	21.1	28.98	73.1	1.1555	91668	y
1.15	31.6	28.98	73.6	1.1543	137145	y
1.15	42.4	28.98	74	1.1534	183879	y
3.2	21.2	28.94	73.4	1.1531	91916	y
3.2	32	28.98	73.5	1.1545	138908	y
3.2	42.6	28.98	73.8	1.1540	184832	y
5.1	21.4	29.32	68.8	1.1785	94827	y
5.1	32.1	29.32	69.4	1.1773	142086	y
5.1	42.9	29.32	69.6	1.1768	189821	y
7.3	21.5	29.32	69.3	1.1774	95180	y
7.3	32.1	29.32	69.5	1.1770	142052	y
7.3	42.8	29.32	69.7	1.1765	189326	y
9.4	21.3	29.32	69.9	1.1762	94195	y
9.4	32	29.32	69.8	1.1765	141546	y
9.4	42.7	29.33	70	1.1761	188814	y
11.4	21.3	29.33	70.1	1.1758	94167	y
11.4	32.3	29.32	70	1.1760	142816	y
11.4	42.6	29.32	70.1	1.1757	188315	y
13.4	21.3	29.32	69.6	1.1768	94246	y
13.4	32	29.32	70.3	1.1753	141405	y
13.4	42.6	29.32	70.3	1.1752	188234	y

Appendix B. Camera Settings

Execute the following checklists to ensure the cameras are synchronized.

To open all three cameras with common format/controls:

1) Run XCAP.

2) From the PIXCI menu, select "PIXCI Open/Close".

3) Click Close if the board is already open.

4) Click "Multiple Devices".

5) Make sure there is a check next to Device#0, Device#1, and Device#2.

6) Select "Use Common Format & Controls w. Cameras Synchronized".

7) Click OK.

8) Click Open.

NOTE: The above 8 steps are how the system is configured at the time of shipping, they are only necessary if software settings have been changed.

To synchronize the cameras and get them running:

1) From the PIXCI menu, select "PIXCI Video Setup" and then "PIXCI Unit 0 Video Setup".

2) Select the Custom tab, then select the "Camera Control" tab.

3) Set "Selected MSSMUB Bits" to 2.

4) Click OK.

5) In the Trig tab of the "Capture & Adjust" window, set the "Camera Exp. Mode" to "EXSYNC Level".

6) In the Trig tab of the "Capture & Adjust" window, select Continuous. Cameras are now running synchronized.

The following list contains instructions on saving image sequences to the hard drive.

To save the image sequences to the hard drive:

1) In the Unit 0 View window, select "Save Image Sequence" from the file menu.

2) Select the format you wish to save the sequence in.

3) Click "Set AOI". Under the AOI tab, you can select which portion of each image to save. The default is to save the entire image. Under the Image tab, you can select which image buffers to save. The default is to save all buffers that were captured into during the last sequence capture.

4) Click Browse, and browse for a location and file name to save the sequence.

5) Click OK to save the image sequence.

6) Repeat steps 1-5 for the Unit 1 View window to save the sequence from Unit 1, then repeat steps 1-5 for the Unit 2 View window to save the sequence from Unit 2.

Appendix C. PhotoModeler® Processing

The following is a list of instructions to analyze a sequence of image sets in PhotoModeler®.

1. Open PhotoModeler®and start a .pmv project.
2. Load the calibration file for each camera.
3. Select the image sequences and associated cameras.
4. Mark the targets using automatic target marking. Ensure the coded target recognition is set to "some".
5. Clean up the target marking.
    - Delete extraneous marks.
    - Mark missed targets using the sub-pixel marking tool.
    - Process the project. This orients the images and auto references the coded targets.
    - Reference any targets that were supposed to be recognized as coded targets but were missed. Associate them with coded targets in the other images.
6. Auto reference the remaining points (non-coded targets). Use a search distance of 0.05 pixels.
7. Scale and rotate the project.
    - Translate- select a target and define its location.
    - Units and Scale- select two points and give their separation distance. The separation distance between targets 1 and 2 is 18.53125 in.
    - Rotate- select two points to define the x-axis and two points to define the z-axis. Points 1 and 3 define the x-axis and points 1 and 2 define the z-axis.
8. Track points through 100 frames (referred to as "epochs" in PhotoModeler®.
    - Select the number of frames to track through.

- Set the search radius to 0.3 pixels. Increase the search radius if several points get dropped from one frame to the next.

9. Switch back to the first epoch and process the project again.
10. Perform an "Epoch 3-D Data Export". This exports the coordinates of all points in each epoch to a text file.

Appendix D. Matlab Code

This appendix contains some of the algorithms used to process the data including the sorting algorithm and the TPS algorithm.

D.1 Sorting the Targets

Listing D.1: Target Sorting Alorithm.(Appendix4/sortdata2.m)

```
function out = sortdata2(data,aoa_ref,speed_ref,wingtype,static)
% sort the x, y, z coordinates by x first, then z
% wingtype can be "f" for flexible or "s" for stiff

% look up actual aoa and speed
[aoa,speed] = aoa_speed(aoa_ref,speed_ref);

% rotate from the current aoa to -6 degrees
clone = data(:,1:3);
ind   = [1:length(data(:,1))]';
% clone is of the form [x-coord y-coord z-coord row#]
clone  = [clone, ind];
rot    = 6 + aoa;
x1     = clone(:,1);
y1     = clone(:,2);
theta1 = atan2(y1,x1)*180/pi;
theta2 = (rot + theta1)*pi/180;
mag    = sqrt(x1.^2 + y1.^2);
clone(:,1) = mag.*cos(theta2);
clone(:,2) = mag.*sin(theta2);

% % sort in the z direction
% % define cutoff values then sort each section
x = clone(:,1);
if wingtype == 's'
    % define cutoff values
    c = [-3.8 -2.5 -1.2 -0.4];
    % define bins based on cutoff values
    bin1 = find(x < c(1));
    bin2 = find(x > c(1) & x < c(2));
    bin3 = find(x > c(2) & x < c(3));
    bin4 = find(x > c(3) & x < c(4));
    bin5 = find(x > c(4));
    % sort the points in each bin by z-coordinate
    m1 = sortmat(clone(bin1,:),3);
    m2 = sortmat(clone(bin2,:),3);
    m3 = sortmat(clone(bin3,:),3);
    m4 = sortmat(clone(bin4,:),3);
    m5 = sortmat(clone(bin5,:),3);
    % final sorted order
    order = [m1(:,4); m2(:,4); m3(:,4); m4(:,4); m5(:,4)];
end
```

```
if wingtype == 'f'
    % define cutoff values
    c  = [-4 -3 -2 -1 -0.2 0];
    if ((aoa_ref >= 10) && (speed_ref >= 30))
        c = [-4 -3 -2 -1 -0.05 -0.2];
    end
    % define bins based on cutoff values
    bin1 = find(x < c(1));
    bin2 = find(x > c(1) & x < c(2));
    bin3 = find(x > c(2) & x < c(3));
    bin4 = find(x > c(3) & x < c(4));
    if (c(6) == 0) || (static == 1)
        bin5 = find(x > c(4) & x < c(5));
        bin6 = find(x > c(5));
    else
        bin5 = find(x > c(4) & x < c(6));
        bin6 = find(x > c(6));
    end
    % sort the points in each bin by z-coordinate
    m1 = sortmat(clone(bin1,:),3);
    m2 = sortmat(clone(bin2,:),3);
    m3 = sortmat(clone(bin3,:),3);
    m4 = sortmat(clone(bin4,:),3);
    m5 = sortmat(clone(bin5,:),3);
    m6 = sortmat(clone(bin6,:),3);
    % final sorted order
    order = [m1(:,4); m2(:,4); m3(:,4); m4(:,4); m5(:,4); m6(:,4)...
       ];
end

% output the final sorted point locations
out = data(order,1:3);
```

D.2 Thin Plate Spline Code

Listing D.2: TPS Alorithm.(Appendix4/splinemat.m)

```
function aero = splinemat(R_a,R_s,delta)
% R_a is the a matrix of aero grid locations
% R_s is the no wind target locations (structural grid)
% delta is the deflection of the targets
% Note: R_a and R_s are both of the form [ones x y z]

% See Appendix A of Parker, Gregory H.,
% "Dynamic Aeroelastic Analysis of Wing/Store Configurations",
% PhD Dissertation, AFIT, 2005

%% Calculate the Thin Plate Spline Transformation Matrix

for i = 1:length(R_a(:,1))
```

```
        for ii = 1:length(R_s(:,1))
            r_as2 = (R_a(i,2) - R_s(ii,2))^2 + (R_a(i,3) - R_s(ii,3))...
                ^2 + (R_a(i,4) - R_s(ii,4))^2; % Parker A.20
            B_as(i,ii) = r_as2*log(r_as2); % Parker A.18
        end
    end

    for i = 1:length(R_s(:,1))
        for ii = 1:length(R_s(:,1))
            r_s2 = (R_s(i,2) - R_s(ii,2))^2 + (R_s(i,3) - R_s(ii,3))...
                ^2 + (R_s(i,4) - R_s(ii,4))^2; % Parker A.21
            B_s(i,ii) = r_s2*log(r_s2); % Parker A.19
        end
    end
    for i = 1:length(R_s(:,1))
        B_s(i,i) = 0; % ensure diagonal elements are zero
    end
    Bsinv = inv(B_s);
    Rst = R_s';
    arg = inv(Rst*Bsinv*R_s)*Rst*Bsinv;

    S = B_as*(Bsinv - Bsinv*R_s*arg) + R_a*arg;  % Parker A.17

    %% Given displacements of the targets, calculate displacement of ...
        the aero grid
    delta_ax = S*delta(:,1);
    delta_ay = S*delta(:,2);
    delta_az = S*delta(:,3);

    q_a0 = R_a(:,2:4);
    aero = q_a0 + [delta_ax delta_ay delta_az];
```

D.3 Airfoil Integration

Listing D.3: Sectional Lift Calculation.(Appendix4/sectionldcalc.m)

```
function [Lift,Drag,ymax] = section_ld_calc(filename,aoa,speed,...
    wing)
% Calculate the sectional lift and drag given the filename ...
    containing the
% sectional pressure data
% The data is stored in the form [x y z p]
% where x, y, z, and p are column vectors with the first row ...
    repeated as
% the last row i.e. x = [x1; x2; ...; xn; x1]

data = dlmread(filename,'',2,0);
data = [data; data(2,:)];     % append the second row to the ...
    bottom of the matrix

% reverse the order of the data as a test
```

```
% order = length(data(:,1)):-1:1;
% data = data(order,:);

x = data(:,1);
y = data(:,2);
z = data(:,3);
p = data(:,4);
% x = [x1; x2; ...; xn; x1; x2].  Similar for y, z, and p

% define i going from 2 through n+1
i = 2:length(x)-1;

% calculate dx and dy as vectors
dx = x(i+1) - x(i);
dy = y(i+1) - y(i);

% calculate the i+1/2 and i-1/2 values
x_i_plus_half = (x(i) + x(i+1))/2;
y_i_plus_half = (y(i) + y(i+1))/2;

x_i_minus_half = (x(i) + x(i-1))/2;
y_i_minus_half = (y(i) + y(i-1))/2;

i = i-1;
% i now goes from 1 through n

%% Calculate the Area of the face from i-1/2 to 1+1/2
Aix = y_i_plus_half - y_i_minus_half;
Aiy = x_i_minus_half - x_i_plus_half;

%% Determine whether the data was exported in a cw or ccw ...
   direction
[ymax, ind] = max(y);
if ind == length(y)
    ind = ind - 1;
end
r = [x(ind+1)-x(ind), y(ind+1)-y(ind), z(ind+1)-z(ind)];
n = [x(ind)-mean(x), y(ind)+10, z(ind+1)-z(ind)];
% if n x r > 0, the data was exported ccw, otherwise it was ...
   exported cw
direction = cross(n,r);
direction = direction(3);

%% Calculate Lift and Drag from L = $\Sigma(A_{iy}*P_i)$, D = $\...
   Sigma(A_{ix}*P_i)$
Lift = -sign(direction)*sum(dot(Aiy,p(i+1)));
Drag = -sign(direction)*sum(dot(Aix,p(i+1)));
```

Appendix E. Gridgen®

This appendix contains detailed steps on building the original grids in Gridgen®.

1. Since the ribs and webbing on the wing were not aligned properly with the carbon-fiber leading portion of the wing, they were translated and rotated to align smoothly.
2. Gaps were filled with database surface patches.
3. Average grid spacing parameter was set to 0.2 in.
4. Domains were created on the fuselage and nose with an Auto Merge Tolerance of 0.1 in and Auto Merge Angle of 7°. Auto Merge was set to join connectors and domains.
5. All database entities were suppressed except those that make up the lower portion of the wing. The domain was built on the lower portion of the wing using an Auto Merge Tolerance of 0.02 in and an Auto Merge Angle of 7°.
6. Step 5 was repeated for the upper surface of the wing.
7. Connectors and domains were created around the edge of the wing.
8. The boundary decay on the wing was set to 0.9 and the minimum edge length to 0.11.
9. The domain on the ruddervator was built using a boundary decay of 0.5 and a minimum edge length of 0.125.
10. The Nighthawk was translated so the center of rotation was located at point [0 0 0].
11. The Nighthawk was rotated to the appropriate angle to represent an AoA listed in Tables A.1 and A.2.
12. A symmetry plane domain was created and scaled by [1 1 0] to ensure it was completely flat.

13. The domains for the wind tunnel were built. The wind tunnel walls were assumed to be inviscid (zero shear) in order to greatly reduce the size of the grid. Accordingly, the average grid spacing was set to 5 in for the wind tunnel walls.
14. The surface grids were exported in a NASTRAN file format.
15. Steps 1 through 14 were repeated for all AoAs listed in Tables A.1 and A.2.

Appendix F. Fluent Scripts

This appendix contains some sample FLUENT®scripts that were used to obtain flow solutions. The following is a list of actions performed by each script.

1. Scale the grid by 0.0254 since the grids were created in inches.
2. Set the viscous model (either laminar or Spalart-Allmaras).
3. Set the operating pressure and density using the wind tunnel measurements. Density was calculated from the wind tunnel measurements using the ideal gas law. It was assumed to be constant for the duration of each wind tunnel run.
4. Set the symmetry plane Boundary Condition (BC) to "symmetry".
5. Set the inlet BC to "velocity-inlet" equal to the velocity measured during wind tunnel testing.
6. Set the outlet BC to "outflow".
7. Set the BC for the wind tunnel walls to "specified shear" with shear = 0.
8. Partition the grid into 4 partitions using Metis.
9. Set residual tolerances to 1e-4.
10. Turn on force monitors for wing surfaces (domains 22-26).
11. Set discretization scheme to 2^{nd} order for pressure and momentum.
12. Set discretization scheme to 2^{nd} order for turbulent kinematic viscosity (for the turbulent solutions).
13. Set pressure under-relaxation factor to 0.15 for the laminar solutions.
14. Initialize the solution to the inlet velocity.
15. Iterate until force monitors have settled.
16. Save the FLUENT®data file and save a FieldViewfile.

F.1 Sample Laminar Script

Listing F.1: Laminar script for 8 degrees AoA and 40 mph. (Appendix6/aoa08speed40fwinglam.script)

```
cat >input << EOF

file/read-case aoa_08_speed_40_fwing_lam.fluent
grid/scale 0.0254 0.0254 0.0254
5
define
        models/viscous/laminar yes
        materials/change-create air air yes constant 1.13690 no no...
            no no no no no no no

10      operating-conditions
                operating-pressure   97721
                reference-pressure-location -0.9398 0 0.0001
                q

15      boundary-conditions

                modify-zone
                        zone-type 39 velocity-inlet
                        zone-type 44 outflow
20                      zone-type 45 symmetry
                        q
                wall 38 no yes shear-bc-spec-shear no 0 no 0 no 0
                velocity-inlet 39 no no yes yes no 18.8204 yes
                copy-bc 38 40 41 42 43
25
                q
        q
parallel/partition/method/metis 4

30 solve
        monitors/residual/convergence-criteria...
            0.0001 0.0001 0.0001 0.0001

        monitors/force
                drag-coefficient yes 22 23 24 25 26 () yes yes "...
                   aoa_08_speed_40_fwing_lam.cd-history" no no...
                    1 0 0
35              lift-coefficient yes 22 23 24 25 26 () yes yes "...
                   aoa_08_speed_40_fwing_lam.cl-history" no no...
                    0 1 0
                q

        set
                discretization-scheme pressure 10
40              discretization-scheme mom 0
                under-relaxation pressure 0.15
                q
```

```
        initialize/set-defaults/x-velocity 18.8204
        initialize/initialize-flow yes
        iterate 100
        q
file/write-case-data aoa_08_speed_40_fwing_lam.fluent-100 yes
file/export/fieldview-unstruct aoa_08_speed_40_fwing_lam-100 ...
   pressure-coefficient x-vel y-vel z-vel vel-mag () yes yes

solve/set
        discretization-scheme pressure 12
        discretization-scheme mom 1
        q
solve/iterate 1400
file/write-case-data aoa_08_speed_40_fwing_lam.fluent-1500 yes
file/export/fieldview-unstruct aoa_08_speed_40_fwing_lam-1500 ...
   pressure-coefficient x-vel y-vel z-vel vel-mag () yes yes
exit y

EOF

fluent 3ddp -t4 -g -i input > aoa_08_speed_40_fwing_lam.fluent.res
```

F.2 Sample Turbulent Script

Listing F.2: Turbulent script for 8° AoA and 40 mph. (Appendix6/aoa08speed40fwingturb.script)

```
cat >input << EOF

file/read-case aoa_08_speed_40_fwing_turb.fluent
grid/scale 0.0254 0.0254 0.0254

define
        models/viscous/spalart-allmaras yes
        materials/change-create air air yes constant 1.13690 no no...
            no no no no no no no

        operating-conditions
                operating-pressure   97721
                reference-pressure-location -0.9398 0 0.0001
                q

        boundary-conditions

                modify-zone
                        zone-type 39 velocity-inlet
                        zone-type 44 outflow
                        zone-type 45 symmetry
                        q
                wall 38 no yes shear-bc-spec-shear no 0 no 0.5 no...
                    0 no 0 no 0
```

```
                velocity-inlet 39 no no yes yes no 18.8204 yes yes...
                    no 0.001
                copy-bc 38 40 41 42 43
25
                q
        q
parallel/partition/method/metis 4

30 solve
        monitors/residual/convergence-criteria...
            0.0001 0.0001 0.0001 0.0001 0.0001

        monitors/force
                drag-coefficient yes 22 23 24 25 26 () yes yes "...
                   aoa_08_speed_40_fwing_turb.cd-history" no no...
                    1 0 0
35              lift-coefficient yes 22 23 24 25 26 () yes yes "...
                   aoa_08_speed_40_fwing_turb.cl-history" no no...
                    0 1 0
                q

        set
                discretization-scheme pressure 10
40              discretization-scheme mom 0
                discretization-scheme nut 0
                q
        initialize/set-defaults/x-velocity 18.8204
        initialize/initialize-flow yes
45      iterate 100
        q
file/write-case-data aoa_08_speed_40_fwing_turb.fluent-100 yes
file/export/fieldview-unstruct aoa_08_speed_40_fwing_turb-100 ...
   pressure-coefficient x-vel y-vel z-vel vel-mag () yes yes

50 solve/set
        discretization-scheme pressure 12
        discretization-scheme mom 1
        discretization-scheme nut 1
        q
55 solve/iterate 1400
file/write-case-data aoa_08_speed_40_fwing_turb.fluent-1500 yes
file/export/fieldview-unstruct aoa_08_speed_40_fwing_turb-1500 ...
   pressure-coefficient x-vel y-vel z-vel vel-mag () yes yes
exit y

60 EOF

fluent 3ddp -t4 -g -i input > aoa_08_speed_40_fwing_turb.fluent....
   res
```

Bibliography

1. "Nighthawk Brochure." Applied Research Associates, Inc.

2. Albertani R., Stanford B., Hubner J. P., Lind R., and Ifju P. "Experimental Analysis of Deformation for Flexible-Wing Micro Air Vehicles." *46th AIAA/ASME/ASCE/AHS/ASC Structures, Structural Dynamics & Materials Conference*. Number 2231. 2005.

3. Barlow J. B., Rae W. H., and Pope A. *Low-Speed Wind Tunnel Testing*. John-Wiley and Sons, 1999.

4. Basler Vision Technologies, 855 Springdale Dr, Suite 160, Exton, PA 19341. *Basler A500k Users Manual* (7 Edition), March 2007.

5. Bertin J. J. and Smith M. L. *Aerodynamics for Engineers*. Prentice Hall, 1998.

6. Black J. T. and Pappa R. S. *Videogrammetry Using Projected Circular Targets: Proof-of-Concept Test*. Technical Report NASA/TM-2003-212148, NASA, February 2003.

7. Cambone S. A., Krieg K., Pace P., and II L. W. *Unmanned Aircraft Systems Roadmap 2005-2030*. Technical Report, Office of the Secretary of Defense, 2005.

8. Carmichael B. H. *Low Reynolds Number Airfoil Survey*. Technical Report, NASA, 1981.

9. Crabtree L. F. "Effects of Leading-Edge Separation on Thin Wings in Two-Dimensional Incompressible Flow," *Journal of Aeronautical Sciences*, *24*:579–604 (1957).

10. DeLuca A. M. *Experimental Investigation into the Aerodynamic Performance of Both Rigid and Flexible Wing Structured Micro-Air-Vehicles*. MS thesis, Air Force Institute of Technology, 2004.

11. DeLuca A. M., Reeder M. F., OL M. V., Freeman J., Bautista I., and Simonich M. "Experimental Investigation into the Aerodynamic Properties of a Flexible and Rigid Wing Micro Air Vehicle." *24th AIAA Aerodynamic Measurement Technology and Ground Testing Conference*. Number 2004-2396. AIAA, June 2004.

12. Donovan J. F. and Selig M. S. "Low Reynolds Number Airfoil Design and Wind Tunnel Testing at Princeton University." *Low Reynolds Number Aerodynamics, Lecture Notes in Engineering 54*, edited by T. J. Mueller, 39–57, Springer-Verlag, June 1989.

13. Duchon J. "Splines Minimizing Rotation-Invariant Semi-Norms in Sobolev Spaces." *Constructive Theory of Functions of Several Variables: Proceedings of a Conference Held at Oberwolfach*, edited by W. Schempp and K Zeller. 85–100. Berlin: Springer-Verlag, April-May 1977.

14. Eos Systems Inc. *PhotoModeler 6 User Guide* (1^{st} Edition), January 2007.

15. Fung Y. C. *An Introduction to the The Theory of Aeroelasticity*. John Wiley & Sons, Inc., 1955.

16. Gaither A., Marcum D., and Mitchell B. "SolidMesh: A Solid Modelling approach to Unstructured Grid Generation." *7th International Conference on Numerical Grid Generation in Computational Field Simulations*. 2000.

17. Gamble B. J. *EXPERIMENTAL ANALYSIS OF PROPELLER INTERACTIONS WITH A FLEXIBLE WING MICRO-AIR-VEHICLE*. MS thesis, Air Force Institute of Technology, 2006.

18. Huber A. F. I. *Death by a Thousand Cuts: Micro-Air Vehicles (MAV) in the Service of Air Force Missions*. Technical Report, Air War College, United States Air Force, April 2001.

19. Ifju P., Jenkins D. A., Ettinger S., Lian Y., Shyy W., and Waszak M. R. "Flexible-Wing-Based Micro Air Vehicles." *40th AIAA Aerospace Sciences Meeting & Exhibit*. Number 0705. January 2002.

20. Lian Y., Shyy W., Ifju P. G., and Verron E. "A Computational Model for Coupled Membrane-Fluid Dynamics." *32nd AIAA Fluid Dynamics Conference and Exhibit*. Number 2002-2972. AIAA, June 2002.

21. Mikhail E. M., Bethel J. S., and McGlone J. C. *Introduction to Modern Photogrammetry*. John Wiley and Sons, 2001.

22. Mueller T. J. *Low Reynolds Number Vehicles*. Technical Report, Advisory Group for Aerospace Research and Development, 1985.

23. Nelson R. C. *Flight Stability and Automatic Control* (2nd Edition). McGraw-Hill, 1998.

24. Pappa R. S., Jones T. W., Black J. T., Walford A., Robson S., and Shortis M. R. *Photogrammetry Methodology Development for Gossamer Spacecraft Structures*. Technical Report NASA/TM-2002-211739, NASA, June 2002.

25. Parker G. H. *Dynamic Aeroelastic Analysis of Wing/Store Configurations*. PhD dissertation, Air Force Institute of Technology, December 2005.

26. Prandtl L. *Applications of modern hydrodynamics to aeronautics*. Technical Report 116, NACA, 1921.

27. Raymer D. P. *Aircraft Design: A Conceptual Approach* (Third Edition). AIAA, 1999.

28. Shyy W., Berg M., and Ljungqvist D. "Flapping and flexible wings for biological and micro air vehicles," *Progress in Aerospace Sciences*, *35*:455–505 (1999).

29. Shyy W., Klevebring F., Nilsson M., Sloan J., Carroll B., and Fuentes C. "Rigid and Flexible Low Reynolds Number Airfoils," *Journal OF AIRCRAFT*, *36*(3):523–529 (1999).

30. Shyy W. and Smith R. "A STUDY OF FLEXIBLE AIRFOIL AERODYNAMICS WITH APPLICATION TO MICRO AERIAL VEHICLES." *28th Fluid Dynamics Conference*. AIAA, 1997.

31. Simpson A., Jacob J., and Smith S. "Flight Control of a UAV with Inflatable Wings with Wing Warping." *24th Applied Aerodynamics Conference*. 2006.

32. Smith M. J., Cesnik C. E. S., Hodges D. H., and Moran K. J. "An evaluation of computational algorithms to interface between CFD and CSD methodologies." *37th Structural Dynamics and Materials Conference and Exhibit*. Number 96-1400. 745–755. AIAA, April 1996.

33. Stanford B., Viieru D., Albertani R., Shyy W., and Ifju P. "A Numerical and Experimental Investigation of Flexible Micro Air Vehicle Wing Deformation." *44th AIAA Aerospace Sciences Meeting and Exhibit*. Jan 2006.

34. Stults J. A. *Computational Aeroelastic Analysis of Micro Air Vehicle with Experimentally Determined Modes*. MS thesis, Air Force Institute of Technology, March 2005.

35. White F. M. *Viscous Fluid Flow* (3 Edition). McGraw Hill, 2006.

36. Wolf P. R. and Dewitt B. A. *Elements of Photogrammetry*. McGraw Hill, 2000.

Vita

Captain Nathan A. Pitcher graduated from high school in Williams Lake, British Columbia. He entered undergraduate studies at the University of Alberta in Edmonton, Alberta where he graduated with a Bachelor of Science degree in Mechanical Engineering in June 2003. He was commissioned through OTS in August 2003.

His first assignment was at Los Angeles AFB where he implemented communications upgrades to the Air Force Satellite Control Network. He entered AFIT in September 2006. Upon graduation, he will be assigned to AFRL/RBAC where he will continue to work in the field of computational fluid dynamics.

REPORT DOCUMENTATION PAGE

Form Approved
OMB No. 0704–0188

1. REPORT DATE (DD–MM–YYYY)	2. REPORT TYPE	3. DATES COVERED *(From — To)*
27–03–2008	Master's Thesis	Sep 2006 — Mar 2008

4. TITLE AND SUBTITLE

A Static Aeroelastic Analysis of a Flexible Wing Mini Unmanned Aerial Vehicle

5a. CONTRACT NUMBER

5b. GRANT NUMBER

5c. PROGRAM ELEMENT NUMBER

6. AUTHOR(S)

Nathan A. Pitcher, Capt, USAF

5d. PROJECT NUMBER

5e. TASK NUMBER

5f. WORK UNIT NUMBER

7. PERFORMING ORGANIZATION NAME(S) AND ADDRESS(ES)

Air Force Institute of Technology
Graduate School of Engineering and Management (AFIT/EN)
2950 Hobson Way
WPAFB OH 45433-7765

8. PERFORMING ORGANIZATION REPORT NUMBER

AFIT/GAE/ENY/08-M23

9. SPONSORING / MONITORING AGENCY NAME(S) AND ADDRESS(ES)

Dr. Mark Mears, AFRL/RBCA
2210 8th St, Bldg 146, Rm 305,
Wright-Patterson AFB, OH 45433-7531
(937) 255-8685

10. SPONSOR/MONITOR'S ACRONYM(S)

11. SPONSOR/MONITOR'S REPORT NUMBER(S)

12. DISTRIBUTION / AVAILABILITY STATEMENT

APPROVED FOR PUBLIC RELEASE; DISTRIBUTION UNLIMITED

13. SUPPLEMENTARY NOTES

14. ABSTRACT

The static aeroelastic behavior of the Nighthawk mini unmanned aerial vehicle is examined using a combined experimental and computational approach. Three wings are examined. In order of increasing stiffness they are: a flexible wing, a stiff wing, and a fictitious rigid wing with zero deflection. Photogrammetry is used during wind tunnel testing to measure the average deflected shape of the flexible and stiff wings during flight. The independent variables during wind tunnel tests are angle of attack (ranging from -5.1° through 13.4°) and velocity, which is 20 mph, 30 mph, and 40 mph. Roll angle and yaw angle are control variables, held constant at 0°. The measured deflection of each wing is used to adjust the wing shape for computational fluid dynamics analysis. Solutions are obtained for the flexible, stiff, and undeflected (or rigid) wings using a steady-state viscous flow solver with a Spalart-Allmaras turbulence model. The flexible and stiff wings experience two forms of deformation during flight. They bend upward along the span increasing the dihedral, and the leading edge twists downward (wing washout). The amplitude of deflection is greatest for the flexible wing. As a result, the flexible wing is more stable, but also exhibits worse static aerodynamic performance. The rigid wing has the greatest lift ($C_{L\,max}$=1.29) and the highest lift-to-drag ratio (L/D_{max} =10.2). Stall occurs first near the root for all three wings. None of the wings stall at the tip in the range of angles of attack tested. A separation bubble forms under the wing at angles of attack less than 8°. This separation decreases the overall lift. It is most prominent on the flexible wing.

15. SUBJECT TERMS

Aeroelasticity, Thin Wings, Photogrammetry, Computational Fluid Dynamics, Subsonic Wind Tunnels

16. SECURITY CLASSIFICATION OF:			17. LIMITATION OF ABSTRACT	18. NUMBER OF PAGES	19a. NAME OF RESPONSIBLE PERSON
a. REPORT	b. ABSTRACT	c. THIS PAGE			Lt Col Raymond C. Maple, PhD
U	U	U	UU	111	19b. TELEPHONE NUMBER (Include Area Code) (937) 255-3636, ext 4577 e-mail: Raymond.Maple@afit.edu